Process Optimization of Robotic Laser Weld Brazing for AI-friendly Dataset Generation to Enable Smart Ultrasonic Inspection of Braze Joint Quality in Industry 4.0

S. Akbarian [*1,2], R. Scott [3], A. Ouellette [3], A. Salandari-Rabori [1,2], S. Sarafan [2], P. Wanjara [2], J. Gholipour [2], E. Hetrick [4], B. Ghaffari [4], R. Maev [3], E. Biro [1]

[1] *Centre for Advanced Materials Joining, Department of Mechanical & Mechatronics Engineering, University of Waterloo, Waterloo, Canada*

[2] *National Research Council Canada, Aerospace Research Center, Montreal, H3T 1J4, Canada*

[3] *Tessonics Inc., Windsor, Canada*

[4] *Research and Innovation Center, Ford Motor Company, 2101 Village Rd, Dearborn, MI, 48124, USA*

[*] *Corresponding author's e-mail address: shima.akbarian@uwaterloo.ca*

Abstract

This study establishes a custom-designed process window for a robotic laser weld brazing (LWB) process to control defects in braze seams used in automotive applications. This window is essential for producing braze seams of varying quality that meet custom specifications, enabling the development of an industrial-level ultrasonic testing (UT) defect detection system, with artificial intelligence (AI) automating UT data processing and measurement extraction. To obtain the required custom samples for training the AI model, a novel wire-adjusted heat input approach was defined, expounding a clear correlation between heat input and defect formation, unlike the traditional nominal heat input, which lacked consistency under varied wire feed speeds. This novel approach enabled precise delineation of heat input-related boundaries to distinguish defect-free conditions from those with lack of adhesion (LoA), pores, base metal melting (BMM), and non-conforming braze geometry. The process window was validated using micro-computed tomography (μCT) to scan and analyze defect distribution along the entire braze seam length. A semi-automated segmentation method was developed to facilitate statistical analysis of defect evolution, ensuring reliable classification of the defects. UT signatures for both defects and seam geometry were evaluated, and reliable signal feedback for defect detection was substantiated. A deep learning model, trained using μCT-derived ground truth, predicted seam geometry directly from UT data, achieving high alignment with μCT measurements across

varied geometries and defects. The process window establishes the groundwork for both UT detection and AI-based geometry prediction, while extending AI-based detection to other defects warrants future investigation.

Keywords: Laser weld brazing; Heat input; Artificial intelligence; Quality control; X-ray Micro-CT; Ultrasonic Testing.

1 Introduction

Robotic laser weld brazing (LWB) has received significant attention in joint design in the realm of modern automated manufacturing [1]. According to Koltsov and Cretteur, this method has mostly been employed for joint assembly, particularly in the joining of roofs and hatchbacks, in luxury lines of well-known car companies such as Ford, General Motors, BMW, Volkswagen, and Renault-Nissan [2]. These applications have been typically brazed because substrate melting in weld brazing processes, in general, are minimized by limiting the input energy to only melt the brazing filler metal, often in the form of wire, to join two or more similar/dissimilar substrates. The processing temperature only needs to exceed the melting temperature (T_m) of the filler metal, which is typically selected to be lower than the T_m of the substrates [3]. The use of laser processing for brazing offers further advantages. LWB joints with narrow filler material offer aesthetically pleasing seamless joint appearance, which makes it an ideal joining method for regions visible to the customer, particularly in assembly of exterior automotive body panels. Moreover, due to the precise energy input and the localized heat generation achieved by the laser heat source, LWB can increase productivity compared to traditional brazing methods, such as gas metal arc brazing (GMAB), by increasing travel speed [4]. These factors make LWB a more energy-efficient choice for automotive brazing. Akbarian et al. [5] reported that LWB achieves nearly twice the joining speed of GMAB while also offering superior precision for intricate details. These advantages are attributed to the higher energy density and greater stability of the laser beam compared to the heat generated by the electric arc in arc welding processes, a behavior consistently observed in arc-based brazing studies [6], with similar observations also described in [7].

Producing high-quality LWB seams requires strategies to minimize the formation of brazing defects during the assembly process. Brazing defects resulting in poor joint appearance are surface defects including cavities, surface-breaking pores, blow holes, spatter, insufficient

wetting, or lack of adhesion, skipping, undercut, and wavy appearance seam [8]. In addition to surface defects degrading joint appearance, sub-surface defects, which cannot be seen from the surface, can significantly limit joint integrity. Porosity, lack of adhesion, incomplete fusion, insufficient penetration, base metal melting, and cracking are common types of sub-surface defects [8]. While surface defects are typically related to issues at the joint's outermost layer, sub-surface defects in laser brazing are often tied to the precise control of heat distribution and penetration within the joint, as well as material interactions and joint design [9].

To inspect sub-surface defects in LWB seams at a manufacturing scale, various non-destructive testing (NDT) methods are employed. These methods include X-ray and micro-computed tomography (μCT) scanning [10], eddy current testing [11], and ultrasonic testing (UT) [12]. Over the last decade, NDT technologies have undergone remarkable advancements through the adoption of artificial intelligence (AI). Representative studies have reported improvements in data interpretation [13], automation [14], and defect characterization [15]–[17]. For NDT applications, modern AI, particularly machine learning (ML) and deep learning (DL), revolve around the use of data-driven algorithms and model architectures designed to replicate or augment human expertise in interpreting NDT data. The convergence of AI and NDT has ushered a new era by aiming toward zero-defect manufacturing by enabling 100% inspection coverage and traceability, real-time monitoring, and predictive maintenance strategies to diagnose the root causes of a detected defect and adjust the variables to resolve the issue instantly without shutting down the process line [18]. This can reduce human error, improve inspection reliability, achieve cost savings, and enhance efficiency. Defect detection using ML and DL often involves framing a signal/image processing stage as anomaly detection [19], classification (identification of a category for a given input) [20], object detection (classifying regions of interest and tightly enclosing them in bounding boxes) [21], while related approaches were further explored in [22]. Semantic segmentation (classification of pixels/voxels in inputs) has also been widely applied for detailed defect characterization, as demonstrated in [23]. Similar use of segmentation-based approaches was also reported in [24]. Though these strategies have proven powerful in NDT applications, including in UT [25], the development and deployment of modern AI approaches has many significant challenges, especially applications such as automotive assembly.

Besides the significant challenges in ML/DL model development and deployment – for example estimating deployed NDT system performance, estimating ML/DL prediction confidence, AI trustworthiness, and data drift – serious complications can arise even earlier in the modeling lifecycle in NDT applications. In particular, as the ML/DL approaches are data-driven, dataset size, dataset coverage, dataset balance, and biases are major concerns that can lead to poor performance and generalization of the AI in NDT systems. Thus, many researchers and developers opt to synthesize data via simulations, which can provide greater control over dataset generation [26]. However, this approach can also yield models that fail to generalize to real applications, because simulations may produce biased or unrealistic datasets if they are not carefully developed and used. It is therefore far more preferable, when possible, to leverage real NDT data from real products, but this comes with significant challenges itself. In particular, many manufacturing processes are extremely expensive to perform, time-consuming, or difficult to replicate – even to produce nominal samples. To achieve sufficient dataset size for NDT defect detection, samples must represent the full range of real production defects. However, creating and verifying such samples through alternative NDT or destructive tests is a significant and often insurmountable challenge. Training AI to enhance real-time NDT requires a robust and reliable database that aligns with manufacturer inspection criteria, such as geometrical factors and defect intensity. It must also provide sufficient dataset variability, quantity, and repeatability.

Achieving zero-defect manufacturing in LWB through real-time quality control systems necessitates the production of braze seams with well-characterized defects for AI training. These defects must be distinctly identifiable across various braze conditions to enable a deeper understanding of their complex origins. Yet, there is no direct reference to optimize the formation of defects that are arising during the LWB process. The most commonly known approach is defining the heat input of the LWB process by the nominal heat input, calculated by dividing the power by the brazing speed—two readily accessible process parameters. Gatzen et al. [27] described nominal heat input using power divided by brazing speed. Lou et al. [28] also used this nominal heat input formulation in LWB process analysis. However, nominal heat input does not account for the remainder of process parameters, such as wire feed speed, wire diameter, and laser beam spot size diameter, which affect the heat necessary to melt the brazing wire and the heat available to raise the temperature of the workpiece to ensure that the molten braze can flow on the substrates. Measurement of the real heat input of the process requires

sophisticated calculation models such as Gaussian-distributed surface heat source modeling based on transient heat conduction [29], inverse heat input estimation using infrared temperature feedback [30], and thermal-field-based reconstruction methods [31]. Process optimization requires a more direct approach to define the process heat input to select principal parameters, such as power, brazing/travel speed, and speed of wire feeding. As an approach to incorporating the wire feed rate into process optimization, the ratio between wire feed rate to travel speed is considered as an indicator, where a higher ratio reduces the risk of substrate mixing due to increased wire deposition [32]. However, no explicit formula has been proposed to define heat input as a unified parameter that simultaneously incorporates power, brazing speed, and wire feed rate. A key knowledge gap is the lack of a robust correlation between the principal LWB parameters and brazing defects, instead of implementing complex heat input models. The dependence of defect formation on heat input is consistent with thermally driven mechanisms governing filler melting, wetting behavior, and substrate interaction in LWB processes. Jin et al. [31] reported a qualitative relationship between heat input–related parameters and microstructural uniformity in LWB joints. Similarly, Zhao et al. [33] discussed the influence of heat input on bonding behavior without providing quantitative correlations. Yang et al. [34] also presented qualitative trends linking heat input metrics to joint characteristics rather than establishing explicit quantitative relationships.

This study addresses the critical challenges of producing braze seams with and without various classes of defects and generating sufficient datasets for AI training, aiming to provide a smart solution quality control for LWB joints in automotive manufacturing. A novel LWB optimization strategy, leveraging heat input-related parameters, was developed to navigate the formation of various sub-surface defects during the LWB of ultra-thin gauges of galvanized interstitial free (GI-IF) steels in roof joint configurations. While the present study focuses on establishing a controlled framework for generating well-characterized defect conditions, practical manufacturing environments may involve additional disturbances such as laser power fluctuations, wire feed instability, and surface contamination (e.g., oil residues or oxide layers). Investigating the robustness of AI-based inspection systems under such process disturbances is considered future work building upon the dataset and optimization strategy developed in this study. To generate comprehensive datasets for AI training, μCT analysis was employed to detect and characterize braze geometry and defects across the entire seam. The AI performance for

predicting braze geometry from UT data, trained using μCT scans, was also evaluated. While μCT scanning has been predominantly applied to single-material samples with simple geometries, its application to characterize defects in multi-material brazed joints with complex geometries remains underexplored. Since braze seams often exhibit variations along the seam, understanding the defect development is critical. The defect evolution was statistically analyzed from μCT scans of LWB joints to ensure compliance with specifications and robustness within the process window. This study offers key insights into optimizing the LWB process in pursuits of AI-assisted zero-defect manufacturing aligning with Industry 4.0.

2 Experimental procedure

2.1 Materials specifications

The material used in this study was thin-gauge, GI-IF steel that was 0.65 ± 0.02 mm thick. The Zn coating had a weight of 50 g/m^2 on both the top and bottom surfaces. The filler material for the LWB process was a Si-bronze, CuSi3Mn1, brazing filler wire with a diameter of 1.2 mm. The chemical compositions of the substrate and filler wire are listed in Table 1.

Table 1. Chemical composition (wt.%) of the GI-IF steel (substrate) and CuSi3Mn1 (filler) wire.

Material	Fe	Cu	C	Si	Mn	P	S	Al
GI-IF	Bal.	-	0.06	0.50	0.40	0.025	0.020	0.010
CuSi3Mn1	0.02	Bal.	-	2.90	0.80	-	-	-

2.2 Roof joint coupon geometry and fixture design

The joint geometry used in the present study was designed to simulate those typical of automotive construction for roof-body applications; so a double-flanged lap joint configuration was used, as shown in Fig. 1. The two coupons used in the joints differ in geometry, most notably in the bending angles of the sheets and there is a height difference of 7 mm between the top surfaces of the substrates. To maintain this distance and ensure high consistency in positioning these parts during LWB, a custom-designed fixture was used [35]. Notably, the acute angle of the roof substrate, combined with the obtuse angle of the body-side substrate and the vertical height difference between the two surfaces, plays a critical role in dictating the braze geometry of the roof joint, as these geometric factors influence how the molten filler flows and solidifies along the seam.

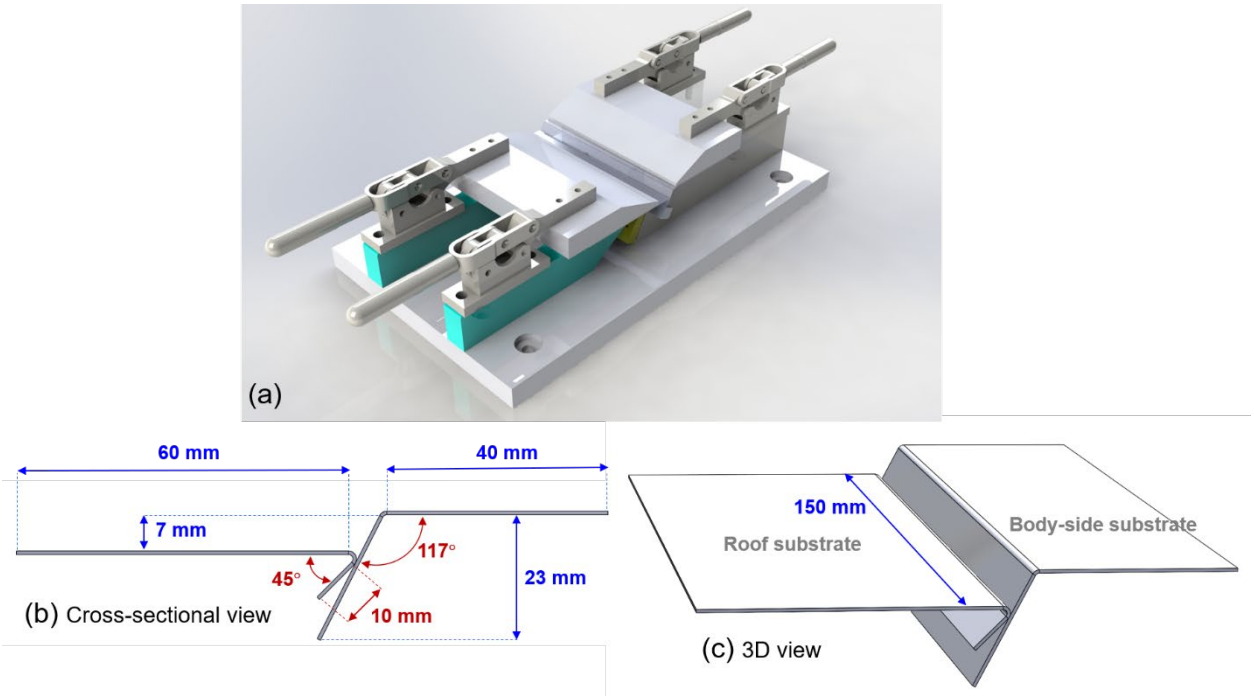


Fig. 1. SolidWorks® CAD model of the (a) custom-designed fixture to clamp the LWB coupons along with (b) 2D and (c) 3D schematics of the LWB coupons for the roof joint configuration.

2.3 LWB process setup

The LWB process was conducted to join the coupons, simulating the body-side and roof in a double-flanged joint configuration. This was performed using a multi-head robotic hybrid laser welder (Lincoln Wayne-Trail/IPG) at the Centre for Advanced Materials Joining (CAMJ) at the University of Waterloo. The facility is equipped with an IPG YLS-8000 fiber laser. The process parameters were selected and optimized to achieve industrially typical brazed joint geometries, while ensuring visually flawless seams on the top surface. For this study, all LWB experiments utilized a laser wavelength of 1070 ± 10 nm. The laser head was equipped with a cold wire feeder; the beam had a waist diameter of a 600 μm and a Gaussian-profile. Brazing was undertaken using a laser beam spot size of 3.2 mm, achieved by defocusing the laser so that the focal point was 42 mm above the workpiece. The laser beam was directed at an incident angle of 90° relative to the substrate (x-y plane), while the filler wire was introduced at a 5° angle, as depicted in Fig. 2a and b. This arrangement for aligning the filler wire, laser beam, and substrate interaction was maintained consistently throughout the experiments.

In keeping with standard industrial practices, no shielding gas was utilized during the brazing process. The primary LWB parameters—power (P), travel speed (TS), and wire feed speed

(WFS)—were varied within the ranges specified in Fig. 2a and b, specifically 2–6 kW, 50−85 mm/s, and 40–80 mm/s, respectively. These operational ranges are representative of those commonly employed in manufacturing. The double-flanged joint configuration resulted in a trapezoidal geometry at the braze seam cross-section [35] after the filler wire melted and solidified, as illustrated in Fig. 2c.

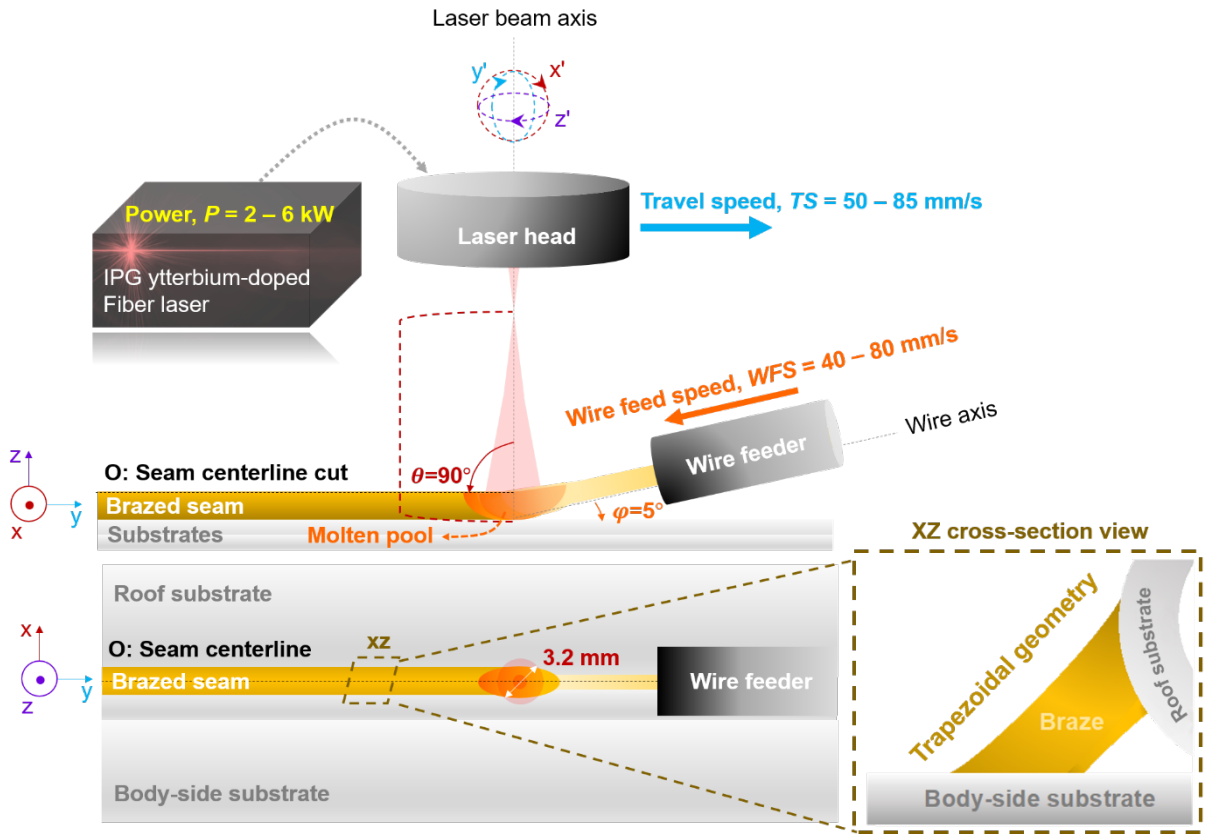
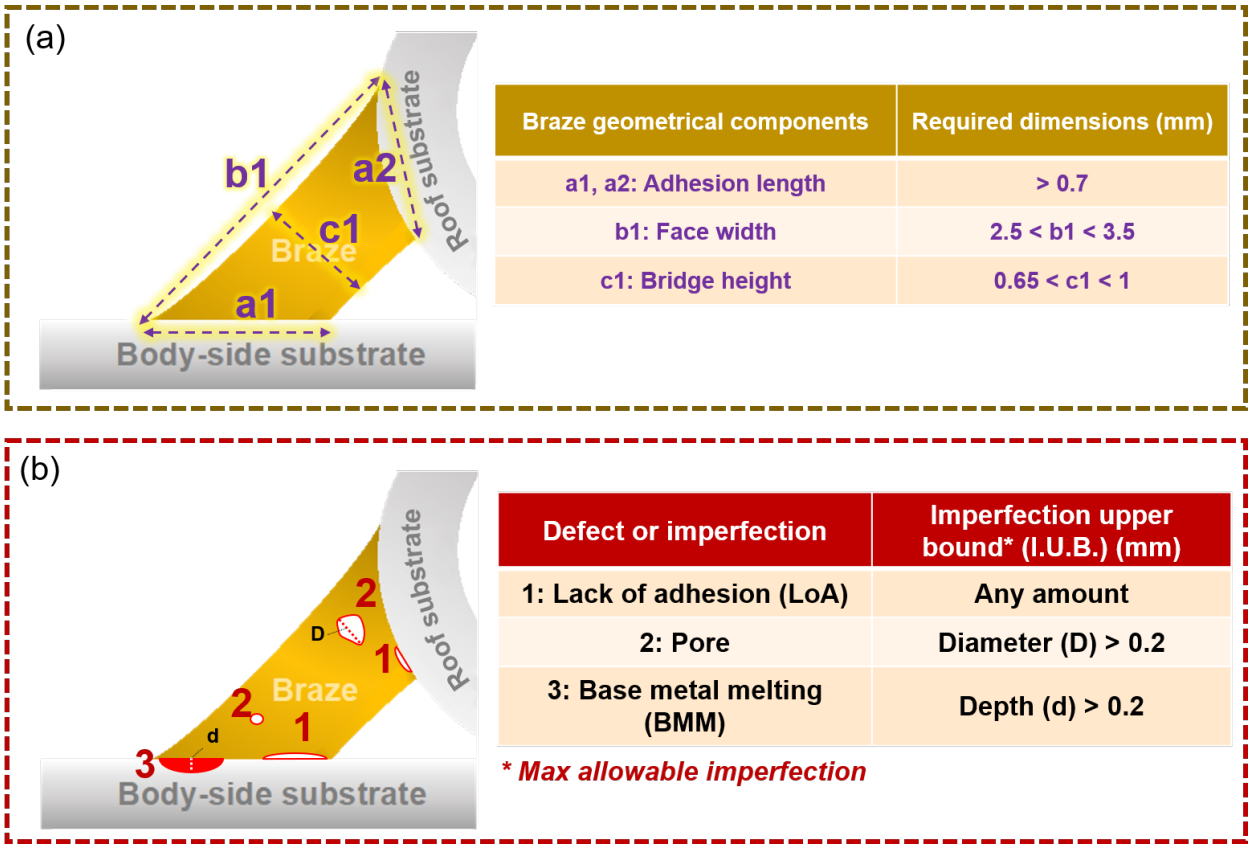


Fig. 2. (a,b) Schematics of the LWB process setup showing non-variables, such as spot size diameter, defocused distance, and the angles of incidence for the laser, wire, and substrate. The experimental domains for principal process variables, including P, TS, and WFS, are also presented; (c) representation of the double-flanged braze geometry.

2.4 AI-friendly specifications

The LWB seams generated for enrichment of the AI development dataset must satisfy certain specifications, including (1) braze geometry and internal imperfections that span the range possible in a manufacturing environment, meaning both below and above the acceptable sizes; and (2) a low variation in the type of imperfections/defects along each braze seam. The target criteria for the braze geometry and imperfections are shown in the tables in Fig. 3. Conforming to these factors enables AI recognition of the braze quality for certain LWB conditions using UT.

Brazing imperfection/defect conditions of interest are non-conforming braze geometries, lack of adhesion (LoA), porosity, and base metal melting (BMM). It is worth mentioning that any manufacturing process will produce imperfections, meaning deviations from the ideal joint properties, but these imperfections were considered as brazing defects only when they exceed the imperfection upper bound (I.U.B.) limits. The I.U.B. limits were defined based on application-specific industrial acceptance criteria established for the intended joining configuration, representing the maximum allowable imperfection sizes beyond which joint performance is considered unacceptable for the targeted service conditions and therefore used as thresholds for defect classification in this study.



Braze geometrical components	Required dimensions (mm)
a1, a2: Adhesion length	> 0.7
b1: Face width	2.5 < b1 < 3.5
c1: Bridge height	0.65 < c1 < 1

Defect or imperfection	Imperfection upper bound* (I.U.B.) (mm)
1: Lack of adhesion (LoA)	Any amount
2: Pore	Diameter (D) > 0.2
3: Base metal melting (BMM)	Depth (d) > 0.2

** Max allowable imperfection*

Fig. 3. AI-friendly specifications for (a) geometry and (b) defect or imperfections detected within the trapezoidal braze geometry of the roof joint.

2.5 Defect characterization

2.5.1 Metallography technique (MT)

The braze microstructure and geometry in each LWB condition were investigated by cross-sectioning the LWB seam perpendicular to the brazing direction. A highly-controlled polishing procedure was used on the four cross-sections extracted from each LWB seam as shown in Fig.

4, according to a metallographic method described in [5]. An optical Keyence VHX-7000 microscope was used to observe the polished cross section surfaces to provide a larger field of view for capturing the whole braze geometry of each cross-section.

2.5.2 X-ray micro-computed tomography (μCT) scanning

To enable a comprehensive analysis of the braze geometry and sub-surface defects, such as pores, μCT scanning was performed on the braze seams under selected conditions. This method plays a crucial role in generating extensive datasets suitable for integration into an AI database. The μCT technology is a computer-based image reconstruction of a series of X-ray images obtained from specified cross-sections, capturing variations in material density, and reconstructed into high-resolution digital 3D images [36]. The density of the tested material is analyzed using the transmission of X-rays, where the reduction in X-ray intensity is quantified by the material's attenuation coefficient, which depends on the material's composition and density. The intensity of X-ray transmitted through an object shows an exponential decay with respect to the density of the tested sample [37]. The μCT outputs a volume of voxels that can be sliced into different gray scale images, with each gray scale number corresponding to the density of the material at a specific position. The greater the material density is, the higher the brightness on the μCT image (white-prone image). By contrast, voids have the smallest density, which will be shown as dark black on the image. This density and structure correlation provides a quantitative method to analyze and reconstruct the full length of each brazed sample based on stacking the μCT images.

The scanner used in this study was a ZEISS Xradia 520 Versa 3D X-ray Nano-CT Scanner at the Multi-Scale Additive Manufacturing Laboratory, at the University of Waterloo. The system includes a 160 kV X-ray source manufactured by Hamamatsu Photonics K.K. with a maximum focal spot size of 4.5 μm. A voxel size of 20 μm was selected to provide sufficient spatial resolution for detecting pores both below and above the I.U.B. To allow for this voxel size, scanning volume was limited to 20 × 20 × 20 mm^3. To fully scan the seam of each braze, samples were first cut using a waterjet machine, as depicted in Fig. 4a to extract μCT samples with a size of 100 × 20 × 20 mm^3 that could fit into the X-ray chamber (Fig. 4b). Then the desired scanning volume was achieved by virtual cross-sectioning, followed by scanning 20 mm long sections, in-turn, from each braze (see Fig. 4c), and measuring the virtual volume as seen in

Fig. 4d. After scanning, the seam was reconstructed using the Zeiss Reconstruction software package, resulting in a series of grayscale images with 16-bit intensity range. Advanced image processing and porosity analysis were performed using Dragonfly Pro v3.1 [38]. Each scan produced 1018 2D slices per 20 mm segment of the braze seam, as illustrated in Fig. 5a. These 2D slices were subsequently processed and stacked to reconstruct the 3D representation of the specimen, as shown in Fig. 5b. For an accurate comparison between the two scans, µCT scans were all cropped to mainly focus on the braze region and its neighboring substrates. The virtual cross-sectioning approach enabled full-length analysis of the braze seam with spatial resolution of 20 µm. Across the full seam length (~100 mm), this resulted in 5090 2D slices per each LWB sample, which were subsequently used for AI training.

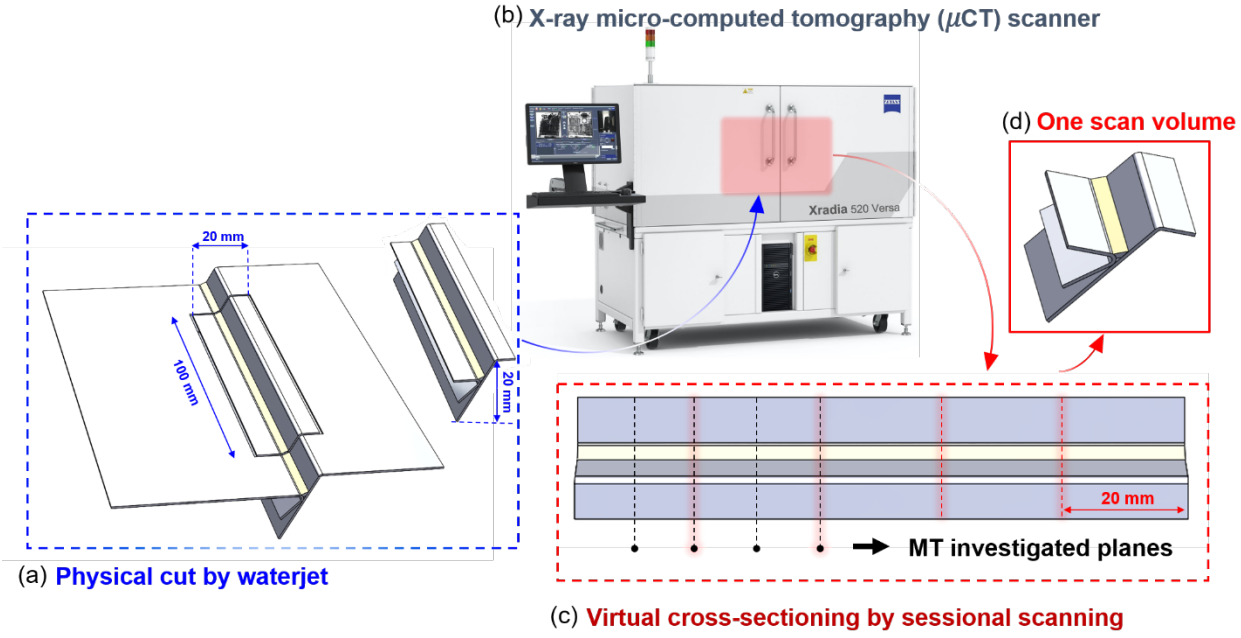


Fig. 4. (a) CAD model of the LWB seam coupon with a roof joint configuration showing the geometry of the extracted sample for µCT scanning, (b) µCT scanning device, (c) virtual cross-section from the full-length (100 mm) µCT scanning sample for each 20 mm length during µCT scanning by dividing into 5 parts, along with indication of the characterized cross-sections for MT, and (d) volume geometry per scan to achieve 20 µm voxel size.

To evaluate the pore formation, a semi-automatic segmentation procedure was used to facilitate detection of pores within the braze seam. Pore identification in the braze joints is challenging because the built-in segmentation modules in DragonFly software may confuse features in the images that arise from the joint geometry with pores (e.g. the space between the braze material and the underlying substrates as shown in Fig. 5a). Additionally, some pores may be missed,

even if they fall within the predefined ranges. For example, as seen in Fig. 5c only a pore with size below 0.04 mm is detected, while the larger pore is missed. To achieve highly accurate pore detection, post-processing of µCT data was initiated with training an automated pore segmentation module and followed by manual correction. Undetected pores were identified and painted within the region of interest (ROI) defined for pores in each 2D slice of the preliminary pore map to ensure that they were properly integrated into the final output. In the final stage, pore quantification, ROIs containing pores smaller than the voxel size were removed from the output. The resulting ROI in Fig. 5d showed that the larger pore size with 0.36 mm diameter is detected, confirming a fully accurate pore detection.

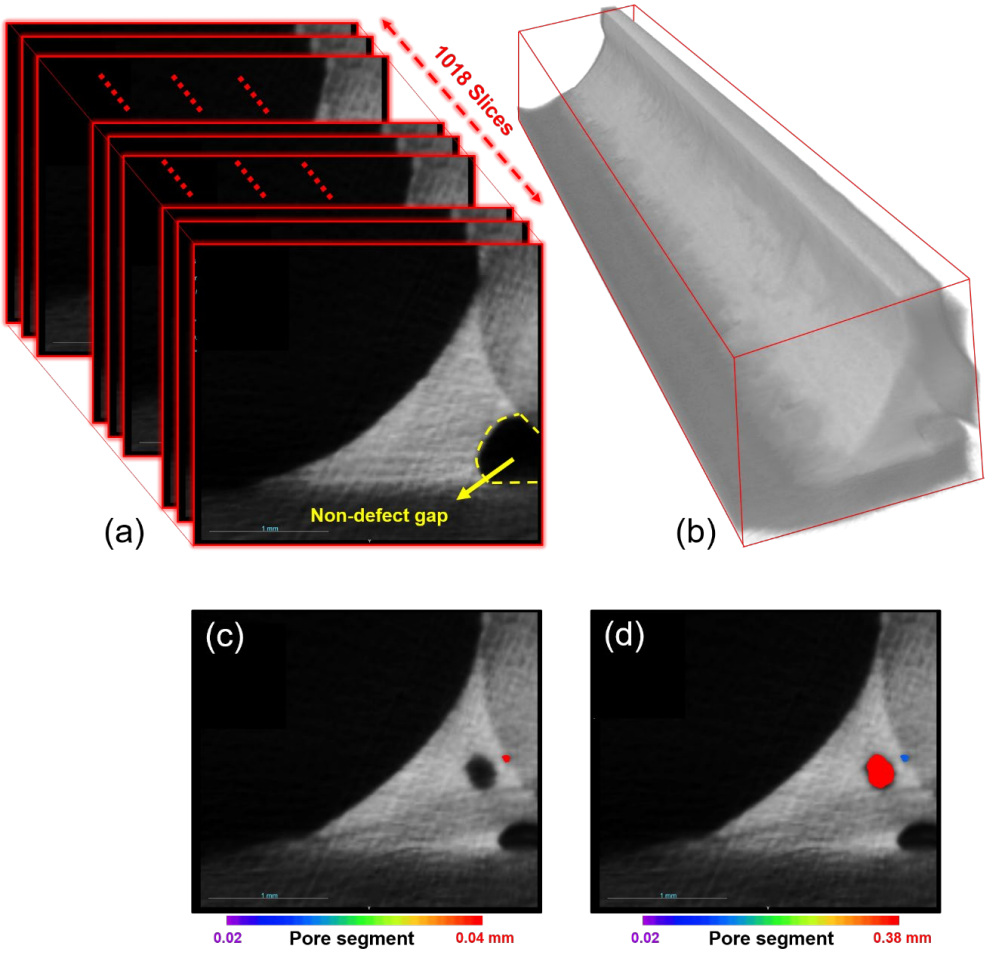


Fig. 5. Post-processing procedure of pore analysis in DragonFly software on µCT data. (a) stacked 2D µCT slices of 1018 for each 20 mm length/portion of the braze seam, (b) 3D processed view of the braze in 20 mm length, (c) example of pore segmentation using an embedded AI module for pore detection in Dragonfly software showing poor pore identification, and (d) manual modification of pore segmentation showing corrected pore identification.

2.5.3 Ultrasonic testing (UT)

To carry out UT of the LWB samples, a methodology based on prior research was used in which samples were sequentially imaged, and the images were reconstructed, similar to the µCT process, where each ultrasonic image is analogous to a cross-section through the sample. Ouellette [11] demonstrated the application of high-resolution phased array imaging for inspection of laser brazed joints. Scott et al. [22] further explored the use of deep learning in interpreting ultrasonic B-scan data. In addition, Ouellette et al. [39] developed full matrix capture approaches for ultrasonic imaging through brazed surfaces, supporting the reconstruction-based imaging methodology used in this study. Here, a linear ultrasonic array placed 10 mm away from the braze surface and is coupled using water as a delay line. For comparison to existing µCT data, a 4 axis isel® Cartesian scanner was used to align the ultrasound probe with the sample and allow for an encoded scan along the direction of the braze. The setup used to acquire the sequential ultrasound images, at a pitch of 0.1 mm, as depicted in Fig. 6a. For each point, a linear 64-element array, with a layout presented in Fig. 6b was used, with properties indicated in Table 2 to acquire the data. This array was chosen based on optimization from previous work [11], [22], [39]. Signals corresponding to each transmit-receive combination of the array elements were acquired for a total of 4096 signal combinations. This data, known as full matrix capture data, was acquired using the commercially available AOS OEMPA mini [40].

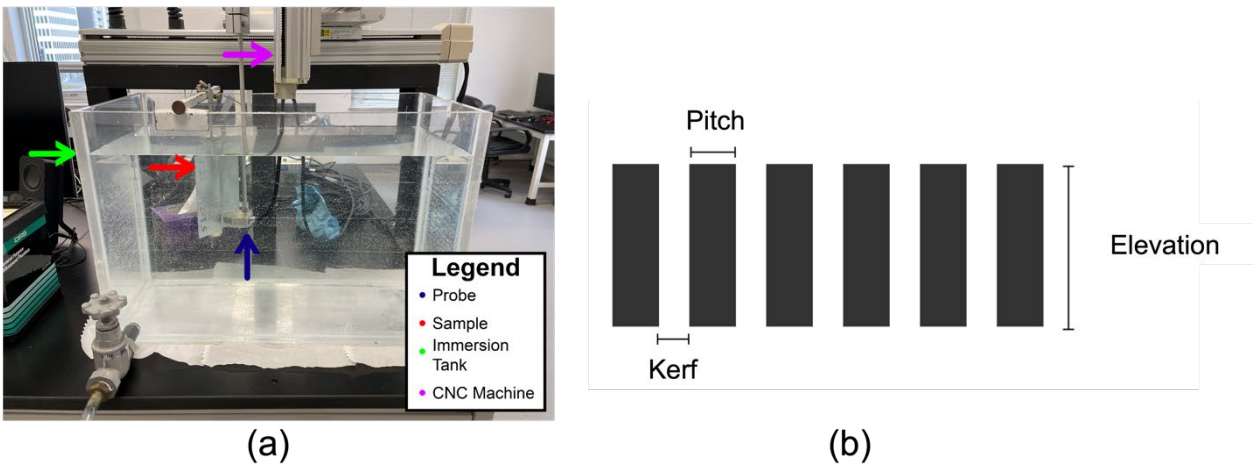


Fig. 6. (a) A picture of the ultrasound acquisition system. Here, a water tank is used to raster the transducer along the LWB samples, acquiring an ultrasonic image of the joint cross section at each point. (b) A depiction of the linear transducer layout and properties.

Table 2. Properties of the ultrasound transducer used in the data acquisition process.

Parameter	Value	Description
Frequency	18.5 MHz	Central frequency of the ultrasonic pulse
Bandwidth	65%	Frequency bandwidth of the transducer, with a higher bandwidth indicating a shorter pulse length
Pitch	0.15 mm	Size of each element in the array along the direction of phasing
Kerf	0.025 mm	Gap between each element in the direction of phasing
Element Elevation	5 mm	Size of the elements in the non-phased direction
Number of Elements	64	Number of elements in the phasing direction
Elevation Focus	15 mm	Ideal imaging depth of the non-phased direction
Beam Size	~0.5 mm	Length of coverage along brazed seam by a single acquisition

This data acquisition method allows for the post processing of acquired data to create an image via the total focusing method using Eq. 1 [25]. Here, the signal emitted at a point, X_n, at a time, t_0, is allowed to propagate through a material using the time evolution operator, H, interact with an observable, O, propagate further, and be recorded at a later time, t, by a receiver located at a position $X_{n'}$. To generate an image at position x and time t, the summation in Equation 1 is applied. It was assumed material properties are temporally invariant during acquisition, so the signal is sampled at a point $t_q + t_{q'}$, corresponding to the most probable path between the emitter and receiver that passes through the point x. This signal is then weighted by the amplitude of the signal expected when the observable is a perfect, point source reflector. By summing all possible transmit-receive pairs, and normalizing by the sum total amplitude, A_{tot}, of all possible paths, a likelihood measure of a reflector being present at position x is computed.

$$< x,t|O|x,t >= \frac{1}{A_{tot}} \sum_{n',n} A_{n'q}, A_{nq} < x_{n'}, t_0 + t_{q'} + t_q|HOH|x_n, t_0 > \quad \text{Eq.1}$$

In this work, this process is performed in a multi-step process [11]. In the first step, the reconstruction is performed in the coupling material, allowing for an analytical computation of the corresponding amplitudes and travel times. In the second step, an estimate of the location of the braze surface is measured, forming a boundary through which sound must pass to interact with the internal structure of the braze. Next, a numerical simulation is performed using an in-

house developed tool to simulate the second order ray series expansion [11], that determines the corresponding travel paths from each emitter to each point in space, while accounting for the effects of the boundary and the acoustic properties of each medium. Using Helmholtz reciprocity, the return path to the receiver is known. Combining the most likely propagation paths in each transmit–receive pair allows for the time-migration function to again be used to form a sub-surface image of the material. In regions where zero or near-zero signals are expected, a value of zero is assigned to prevent singularities. The computation of multiple images along the braze seam allows for a volume of ultrasonic data to be obtained. In order to allow for comparison to μCT data, a rigid body image registration algorithm was developed to allow for 3D alignment of the two data sets.

2.6 AI-based analysis of UT data

Extraction of the joint geometry and defect indications from UT data was framed as a supervised semantic segmentation task, wherein each pixel in the input ultrasonic data is designated a class, such as braze seam, substrate, pore, LoA, and BMM indication, and models are optimized given corresponding ground truth for each given input. To this end, brazed joints, substrate sheets, pore indications, and LoA indications were segmented in the high-resolution μCT scan data from 20 LWB samples with 10 cm length to derive a set of masks of the different classes for each individual μCT image. To enable the transfer of μCT-based ground truth data to the UT dataset, μCT scans, μCT-based masks, and UT scans were aligned using cross-correlation of front and back surfaces of the brazed joint regions. The μCT scans were acquired with a voxel size of 20 um, while each UT image aggregates information within the ultrasonic beam size (0.5 mm) along the braze direction. Therefore, to put the μCT and UT data on the same footing, a set of 25 μCT scans were mapped to the corresponding UT scan, and the UT ground truth for semantic segmentation was the average of the masks for the corresponding 25 μCT scans as seen in Fig. 7.

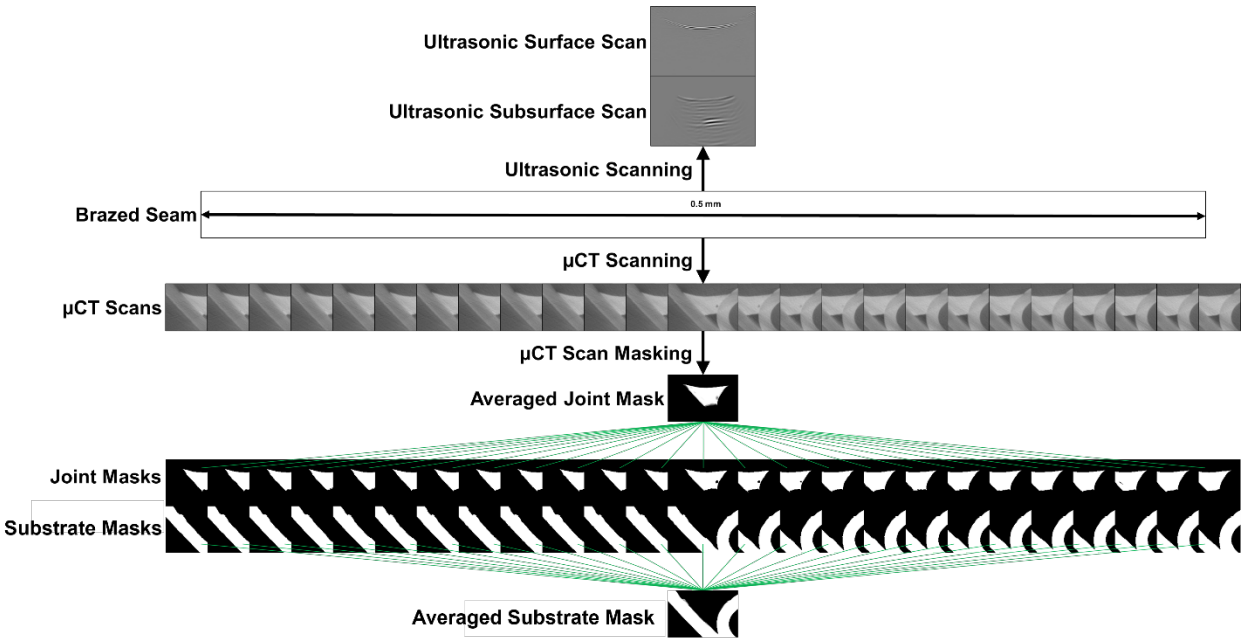


Fig. 7. Mapping of µCT data to corresponding ultrasonic scans along the brazed seam. For each 0.5 mm UT scan (matching the ultrasonic beam size), 25 µCT slices were averaged to generate a single aggregated ground truth segmentation mask representing joint and substrate features.

Semantic segmentation models were based on the U-Net [41] architecture. The models were optimized and trained using ultrasonic images as input and their corresponding aggregated ground truth masks as target outputs. Specifically, for a single inspection position, the input ultrasonic data were a depthwise stacking of the original ultrasonic waveforms and their envelopes, as well as sine and cosine of instantaneous phase, for both the surface and subsurface ultrasonic scans as described in Section 2.5.3. A nested cross-validation approach was used, where the dataset was partitioned based on the joint sample rather than random image slices. Models were evaluated on joints that were held out from model training within the outer cross-validation folds. Both ground truth (from µCT) and AI-based (from UT) mask outputs of the LWB samples were post-processed to enable the extraction of measurements that are often subject to acceptance criteria, as well as comparison between the approaches. Extracted measurements along the joints were smoothed using rolling median.

3 Results and discussions

3.1 LWB process window design using MT

To identify the optimal conditions for producing AI-friendly LWB seams, a comprehensive screening process was performed using OriginPro software. A full factorial design of

experiments (DOE) was generated with a randomized design to maximize the degrees of freedom in selecting LWB parameter sets. Three factors—*P*, *TS*, and *WFS*—were considered, each with multiple levels: 3 for *P*, 3 for *TS*, and 4 for *WFS*. These levels were constrained within the ranges specified in Fig. 2. The blue spheres in the 3D plots in Fig. 8a illustrate the parameter combinations used in the study. Defects were evaluated across four cross-sections per braze joint, and the results were averaged. The 95% confidence interval represents the spread of the values. In cases where the targeted imperfection was inconsistently observed across sections, the resulting larger CI indicates this variability.

The blue spheres with green halos, conditions a-h in Fig. 8a, highlight the preliminary screening window of conditions that meet the AI-friendly specifications for geometry limits and defect classifications. Five classes of LWB conditions were identified by MT: defect-free, LoA, brazes with pore formation below and above 0.2 mm in diameter, and brazes with BMM that was less than 0.2 mm in depth. These conditions namely, “a” to “h”, are represented by corresponding symbols in the bracket tree in Fig. 8a.

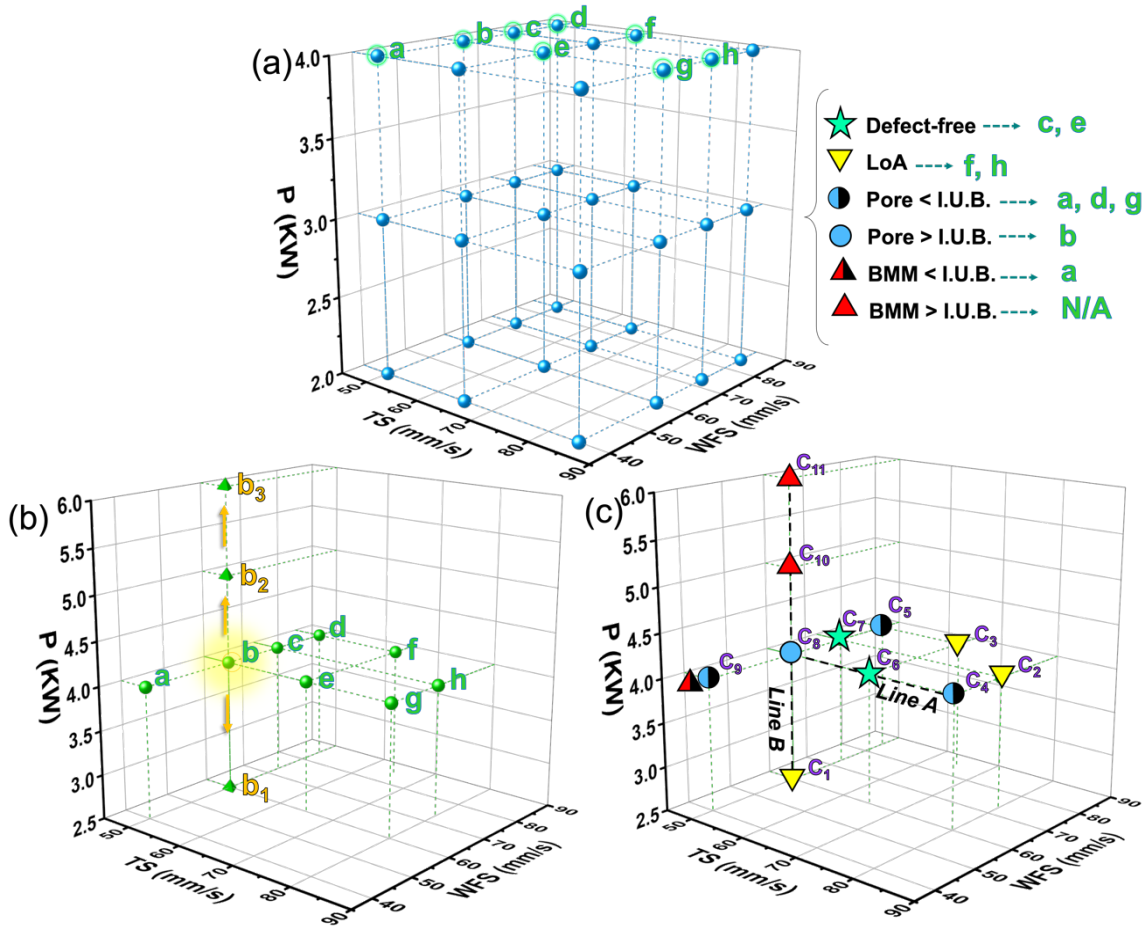


Fig. 8. 3D plots of LWB process window of principal variables, including P, TS, and WFS (a) preliminary screening window with partially achieved defect conditions as highlighted by the green halo, and (b) modified window by embedding new points "b_1", "b_2", and "b_3", (c) resulting LWB window which passed AI-friendly geometrical and defect specifications experimentally.

The LWB parameters causing BMM greater than 0.2 mm (BMM defect) have not yet been achieved from the preliminary screening window in Fig. 8a. To explore LWB conditions which accelerate melting of the base metal, condition "b" from the preliminary screening window was selected. This condition, "b", contains the most severe defects such as large pores (above the pore I.U.B), which formed under an increased heat input. By further adjusting the heat input relative to condition "b", moving to points above and below point "b" in Fig. 8b—where *TS* remains constant—a wider range of defects is expected. Condition "b" was selected because the formation of large pores is a sign of high instability in the braze molten pool, increasing the likelihood of defect formation. It was observed that condition "b_1" with reduced *P* (2.5 kW), led to LoA defects in the brazing seam, even though the *TS* was the lowest level within the modified

window. Conversely, increasing the P to 5 and 6 kW, conditions "b_2" and "b_3", respectively, resulted in BMM exceeding I.U.B. for BMM, 0.2 mm.

The resulting window from MT, encompassing all required defect conditions satisfying the given AI-friendly specifications (as specified in Fig. 3), is depicted in Fig. 8c, in which the achieved conditions are indexed by C_i labels. To avoid presenting identical defect conditions, six points showcasing defect-free and defect conditions such as C_1, C_4, C_6, C_8, C_9, and C_{11}, are considered for further investigation in this study and their corresponding micrographs are gathered in Fig. 9. It is important to emphasize that all achieved conditions exhibited no surface defects in the brazing seam, and the braze geometry using MT measurements conformed to the limits specified for AI-friendly samples. A detailed summary on the braze geometry measurements of candidate conditions is provided in Table 3. Subsequently, µCT analysis was conducted on the produced LWB seams within the resulting MT-defined process window, enabling full-scale characterization of the braze seam geometry and sub-surface defects from along the entire length of the seam.

Table 3. Braze geometry measurements (from MT) of candidate conditions showing AI-friendly geometry specifications passed successfully.

Candidate *Ci*	Bridge height, c1 [mm]	Adhesion length, Body side, a1 [mm]	Adhesion length, roof, a2 [mm]	Face width, b1 [mm]	Passed ?
C_1	0.73 ± 0.08	1.61 ± 0.07	0.87 ± 0.12	2.33 ± 0.11	Yes
C_4	0.59 ± 0.09	1.33 ± 0.28	0.77 ± 0.10	2.09 ± 0.25	Yes
C_6	0.72 ± 0.25	1.83 ± 0.23	1.11 ± 0.16	2.41 ± 0.22	Yes
C_8	0.83 ± 0.05	2.11 ± 0.17	1.16 ± 0.20	2.50 ± 0.34	Yes
C_9	0.73 ± 0.09	2.27 ± 0.43	1.17 ± 0.37	2.65 ± 0.51	Yes
C_{11}	0.78 ± 0.26	2.66 ± 0.34	1.28 ± 0.49	3.30 ± 0.30	Yes
AI-friendly specification	≥ 1	> 0.7	> 0.7	2.5< b1 <3.5	

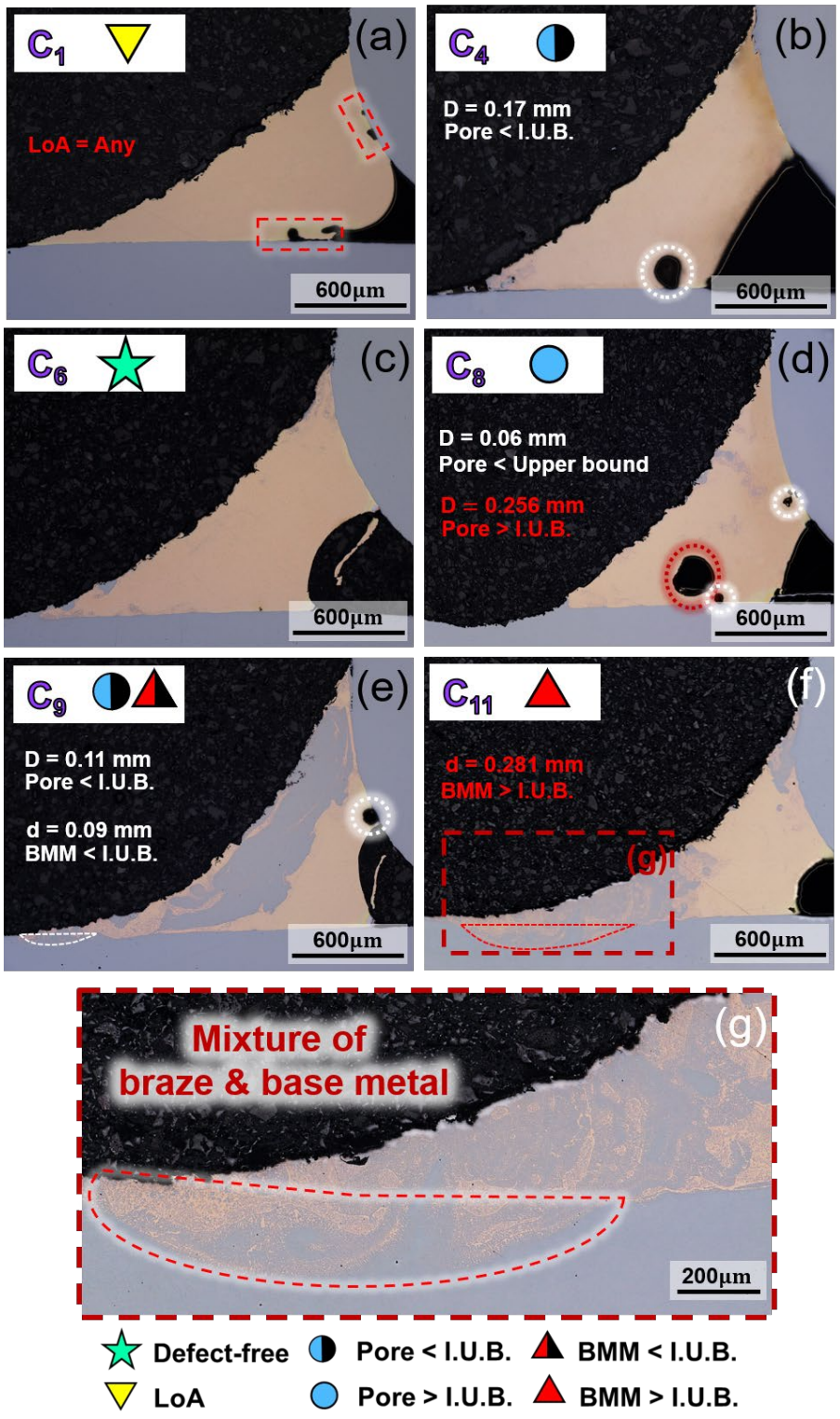


Fig. 9. Braze microstructure of LWB conditions satisfying AI-friendly specifications on geometry and defects. Condition indexes and defect symbols are with respect to Fig. 8c. Imperfections with a size below and above (defect) the I.U.B. are labeled using white and red annotations, respectively.

3.2 A Novel heat input-related approach for LWB defect optimization

To determine the correlation between the different defect classes and LWB variables, the process parameters laying along two lines within the AI-friendly process window in Fig. 8c were isolated to minimize changing parameters. These selections were made to analyze conditions with constant *P* and *WFS* (in line A), and conditions with constant *TS* and *WFS* (in line B). This comparison was based on the nominal heat input ($HI_{Nominal}$), as defined in Eq. 3.1. $HI_{Nominal}$ is the conventional method for presenting heat input for laser brazing [27]. It should be noted that the heat-input framework used in this work is developed for the specific LWB configuration investigated here, including the base metal system, joint geometry, coupon design, and constant laser processing conditions. While the correlations between heat input and defect formation reported in this study are therefore configuration-dependent, the underlying heat-input–based optimization approach has also been demonstrated in our previous work [42] as an effective approach for controlling thermally driven phenomena, such as the formation of intermetallic compounds within the braze region under a different joint configuration.

$$HI_{Nominal} = P/TS \qquad \text{Eq. 3.1}$$

Line A, including C_8, C_6, and C_4, was graphed using $HI_{Nominal}$ plotted against *TS*, as shown in Fig. 10a. As $HI_{Nominal}$ increases by reducing *TS*, various defect classes emerge within this regime. At the lowest *TS* (50 mm/s) in C_8, the braze seam exhibited large pores measuring 0.26 mm, exceeding the pore I.U.B. (0.2 mm). The increase in pore size in C_8 can be attributed to two primary causes. Firstly, the prolonged laser beam exposure time, due to its lower *TS* (compared to C_6 and C_4), leads to excessive vaporization of metals, Zn-coating, and moisture that forms large bubbles and produces gases which can be trapped during solidification. Xia et al. [30] reported that gas trapping in the braze during solidification results in pore formation. Secondly, although brazing at lower *TS* diminishes the solidification rate, the braze still solidifies faster than the escape rate of large bubbles, due to the increased volume of trapped gas in the molten braze. Increasing the *TS* to 65 mm/s in C_6 eliminated defect formation, including pores. Despite the higher solidification rate caused by the increased *TS* compared to C_8, the vaporization rate of Zn and the associated fume generation were effectively reduced, preventing the formation of pores and other defects. However, further increases in the *TS* to 80 mm/s in C_4 led to pore formation again, but these pores were smaller, 0.113 mm, which is below the pore I.U.B. (0.2 mm). The appearance of pores in C_4 confirms that vaporization of metals, Zn-coating, and

moisture can still occur even at high *TS* where $HI_{Nominal}$ is low. However, pore formation in C_4 can be attributed to degraded adhesion and wettability, primarily caused by the increased solidification rate resulting from the shorter laser beam exposure time at high *TS*; this condition represents a critical threshold where the initiation of LoA defects occurs. C_6, with no defects or pores, can be identified as the optimal setting where vaporization and solidification rates are balanced. Thus, by correctly setting the *TS* or laser exposure time, pore development can be effectively controlled.

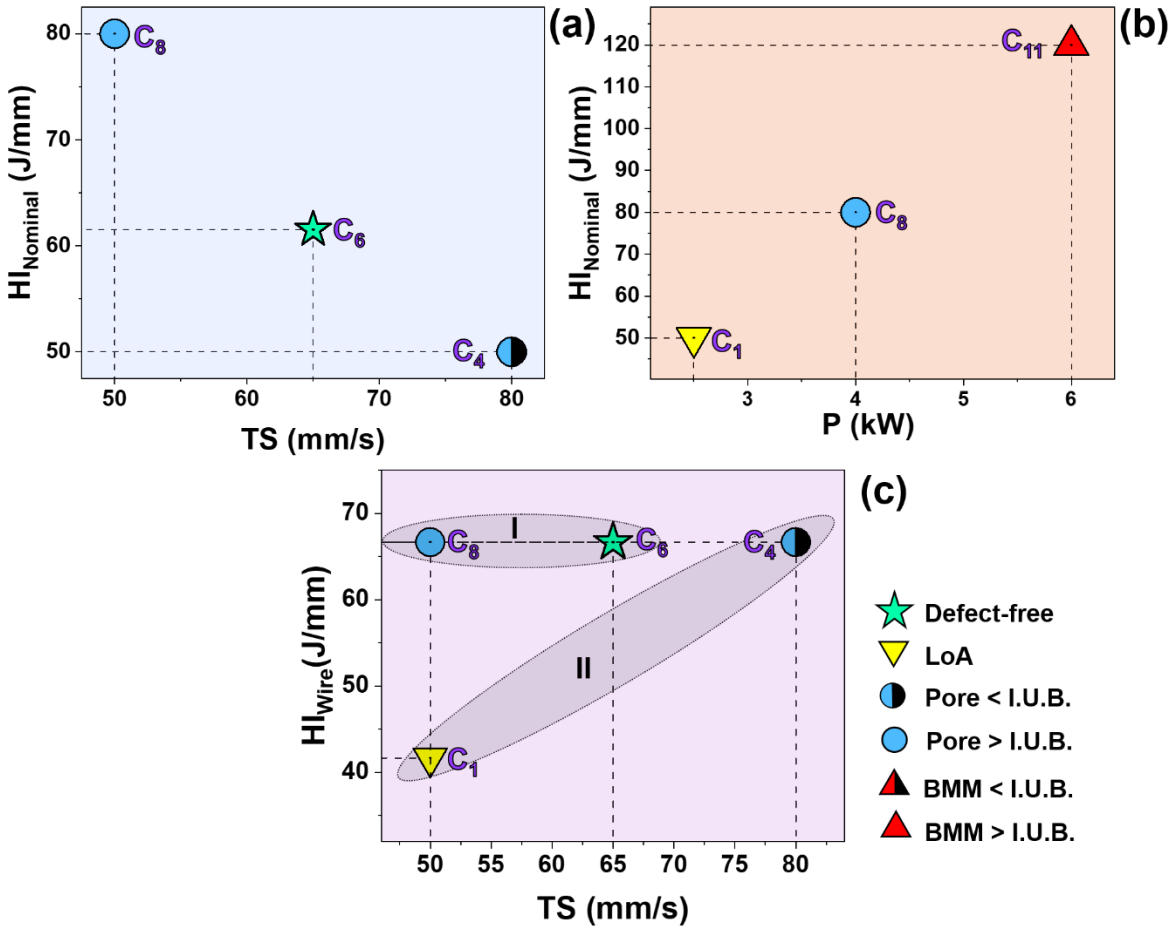


Fig. 10 Correlations between defects and $HI_{Nominal}$ change via (a) *TS* and (b) *P*. (c) Exploring the effect of HI_{Wire} under changing *TS* on defect development.

Line B, which includes conditions C_1, C_8, and C_{11}, reveals the effect of *P* on $HI_{Nominal}$ and defect development, as shown in Fig. 10b. In C_1, with a power setting as low as 2.5 kW (the lowest $HI_{Nominal}$ in this regime), insufficient melting of the braze material at the bottom of the braze root interrupted bonding at the interface, causing a LoA defect. Increasing *P* to 4 kW and 6 kW, in C_8

and C_{11}, respectively, prevented the LoA defect but promoted the formation of large pores in C_8 and BMM in C_{11}, respectively. As revealed from the comparison in Line A in Fig. 10a, the C_8 condition with the lowest *TS* caused the formation of large pores due to the prolonged exposure time of the laser beam. In Fig. 10b, the comparison in Line B further indicates that the increased linear energy delivery, resulting from the higher *P* in C_8 compared to C_1, also contributed to the formation of large pores exceeding the upper bound. The occurrence of the BMM observed in C_{11} resulted from surpassing the process temperature beyond the T_m of the base material. This caused the incorporation of base material into the braze region, which facilitated the diffusion of the braze into the base metal, resulting in deep penetration that exceeded the upper limit for the BMM defect.

In the above discussed conditions, pores, LoA, and BMM are all found to be affected by $HI_{Nominal}$ under different *P* and *TS* levels. The lingering question is, how does *WFS* contribute to this result? The *WFS* is constant in these conditions but in relation to *P* and *TS* it is changing. To investigate this matter, a *HI*-related parameter called wire heat input (HI_{Wire}) is defined as the ratio of *P* to *WFS* in Eq. 3 [35], which is irrespective of the *TS* of the laser torch; this *HI*-related component is a simplification for the heat required to melt the filler wire under the assumption of considering laser as a stationary heat source.

$$HI_{Wire} = P/WFS \qquad \text{Eq. 3}$$

$HI_{Nominal}$ has been extensively used in the literature to date, while HI_{Wire} has not been considered in the interpretation of the heat input in LWB, so it is worthy to investigate how it contributes to defect formation. The LWB conditions resulting in different defect classes were graphed in terms of HI_{Wire} vs. *TS* which revealed two types of correlations, separated in two groups, I and II, as shown in Fig. 10c. For the sake of elucidating each brazing condition comprehensively, a wire-adjusted *HI* term noted by $C_{i=1,2,3,..,n}$ is defined to collect all three *HI* components in 2D space as described in Eq. 4.

$$C_{i=1,2,3,..,n} : (HI_{Nominal}, HI_{Wire})_X \qquad \text{Eq. 4}$$

In group I, C_8:(80 J/mm, 66.6 J/mm)$_{Pore>Thr.}$ and C_6:(61.2 J/mm, 66.6 J/mm)$_{defect\text{-}free}$ both use equal amount of HI_{Wire} but with different $HI_{Nominal}$. In contrast, group II compares C_1:(50 J/mm, 41.6 J/mm)$_{LoA}$ and C_4:(50 J/mm, 66.6 J/mm)$_{Pore<Thr.}$, with equal $HI_{Nominal}$ and varied HI_{Wire}. In group I, the formation of pores with a size above the threshold has been promoted, due to the

excessive $HI_{Nominal}$, while C_1 in group II experienced LoA due to the insufficient HI_{Wire}. In fact, it can be concluded that pore formation is sensitive to $HI_{Nominal}$, while LoA is sensitive to HI_{Wire}. However, this method of assigning two components for heat input to identify each condition's defect classes may not be effective. Analyzing the correlations between each braze defect condition and the *HI* components ($HI_{Nominal}$ and HI_{Wire}) suggests that there might be another component that can relate all these factors together, called relative heat input ($HI_{Relative}$). This component, described in Eq.5 [35], determines the heat delivery to the laser/wire/substrate interaction zone at a relative process speed, Eq.6 [35], as follows:

$$HI_{Relative} = P/V_{Relative} \quad \text{Eq. 5}$$

$$V_{Relative} = TS + WFS \quad \text{Eq. 6}$$

The units for all HI-related components in Eq. 2-6 are expressed in Joules per unit of travel distance. The $V_{Relative}$ in Eq. 5 and Eq. 6 is defined as the sum of TS and WFS, where an increase in either parameter reduces the amount of heat transferred to the system. It was observed that each brazing condition, in relation to the defects, occurs at a specific value of $HI_{Relative}$. Such a correlation could not be identified by relying solely on $HI_{Nominal}$ and HI_{Wire} values. The contour map in Fig. 11 provides a comprehensive overview of the correlations between *HI*-related components and various brazing conditions. The contoured axis in Fig. 11 represents the deviation of the $HI_{Relative}$ of each condition (X) with respect to the $HI_{Relative}$ of the defect-free condition, which is found to be 32 J/mm, as indicated in Eq. 8 [35]. To elucidate each brazing condition comprehensively, the wire-adjusted *HI* term in Eq. 4 was revised to conform to a 3D space, as described in Eq. 8 [35].

$$\Delta HI_{Relative} = (HI_{Relative})_X - (HI_{Relative})_{Defect\text{-}free} \quad \text{Eq. 7}$$

$$C_{i=1,2,3,..,n} : (HI_{Nominal}, HI_{Wire}, \Delta HI_{Relative})_X \quad \text{Eq. 8}$$

Using $\Delta HI_{Relative}$ made navigating through each brazing condition straightforward and consistent. This method can predict which defect condition may arise under a specific LWB condition based on the corresponding $HI_{Relative}$, avoiding the confusion of the two other *HI* components. All conditions and corresponding HI-related parameters are summarized in Table 4. It should be noted that $HI_{Relative}$ depends on the wire diameter and, therefore, cannot serve as a universal measure. To achieve that, the heat of melting for the filler addition must be calculated, which is beyond the scope of this work.

The yellow lines in Fig. 11 delineate the boundaries where each brazing defect forms. The LoA defect is particularly prone to occur at a $\Delta HI_{Relative}$ of −5.33 J/mm, transitioning, as it increases to −3.42 J/mm, to pores with sizes below the threshold. Both conditions sit well below the defect-free condition where $\Delta HI_{Relative}$ is zero. By contrast, positive deviations from the defect-free condition led to the formation of larger pores and BMM defects. For instance, at 4.36 J/mm, there is a significant driving force available to form pores with sizes beyond the pore I.U.B. (0.2 mm diameter). With further deviation to 12.44 J/mm, the pore sizes reduce, but the BMM defects start to emerge with depths below the BMM I.U.B. (0.2 mm depth). At 22.54 J/mm, BMM defects exceed their threshold, defining the BMM defect formation region within this optimization scheme. Although the $HI_{Relative}$ and $\Delta HI_{Relative}$ values are not the exact amount of energy input being used or required for the aforementioned conditions, they can be considered as references to set explicit boundaries distinguishing between each defect formation condition to facilitate LWB optimization when looking for certain defect formation condition(s).

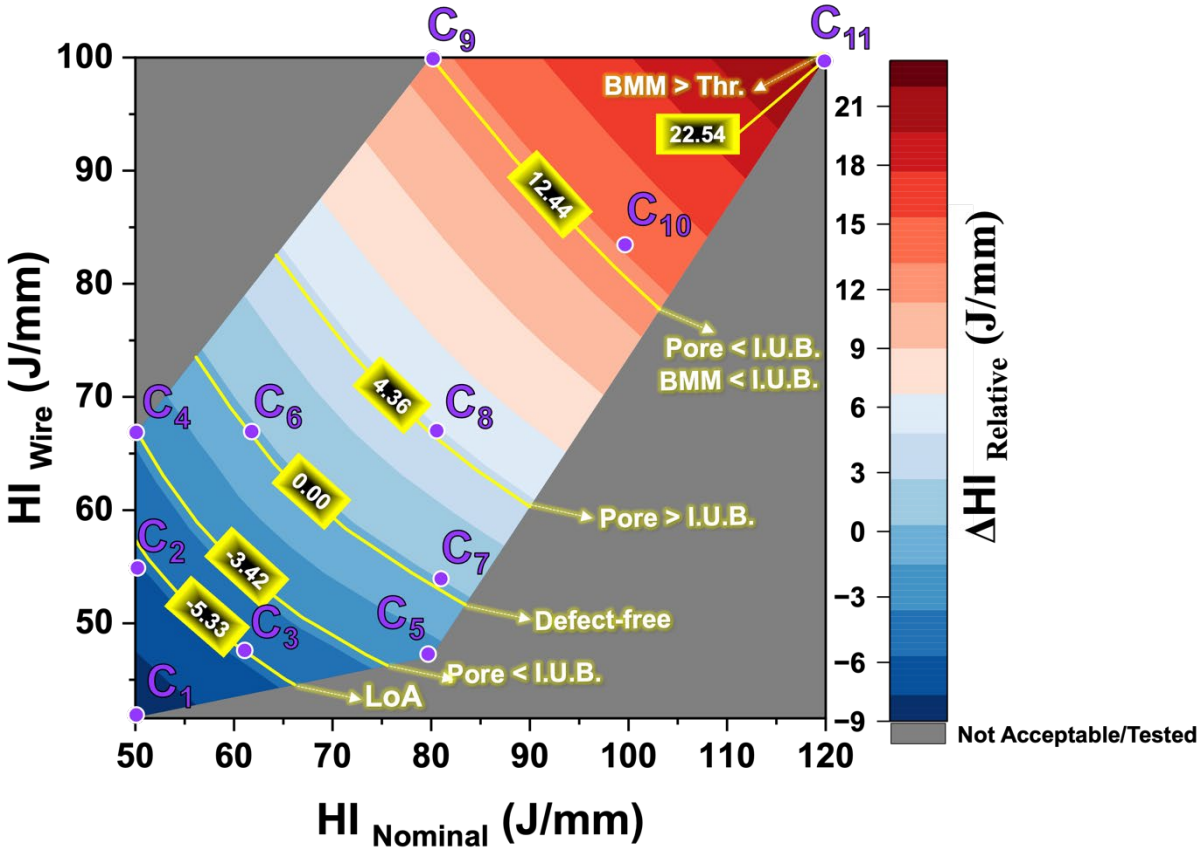


Fig. 11 LWB process road map showing the correlation of heat input-related parameters with various defects conditions.

Increased heat inputs and their impact on pore size have been extensively explored for laser welding; Atabaki et al. [43] reported a transition from small to larger pores with escalating energy levels. This aligns with the present findings that showed that an increase in $\Delta HI_{Relative}$ from −3.42 to 4.36 J/mm leads to an increase in pore size. However, in the present study, it was found that a further increase in the $\Delta HI_{Relative}$, *i.e.*, an increase from 4.36 to 12.44 J/mm, reduces the pore size, where the BMM defect also starts to occur. This raises the question of why pores with a size below the pore I.U.B. (0.2 mm diameter) form at both negative and positive deviations in heat input.

Table 4. Summary of the LWB principle and HI-related parameters.

Ci=1,2,3 ,..,n	*P* (kW)	*TS* (mm/s)	*WFS* (mm/s)	$HI_{Nominal}$ (J/mm)	HI_{Wire} (J/mm)	$HI_{Relative}$ (J/mm)	$\Delta HI_{Relative}$ (J/mm)
C1	2.5	50	60	50	41.67	22.72	−9.27
C2	4	80	73	50	54.79	26.14	−5.85
C3	4	65	85	61.54	47.06	26.66	−5.33
C4	4	80	60	50	66.67	28.57	−3.42
C5	4	50	85	80	47.06	29.63	−2.37
C6	4	65	60	61.54	66.67	32	0
C7	4	50	73	80	54.79	32.52	0.52
C8	4	50	60	80	66.67	36.36	4.36
C9	4	50	40	80	100	44.44	12.44
C10	5	50	60	100	83.33	45.45	13.45
C11	6	50	60	120	100	54.54	22.54

At lower heat inputs, when $\Delta HI_{Relative}$ is −3.42 J/mm (C_4), the laser energy is insufficient to fully melt the filler material, resulting in incomplete wetting of the joint surfaces. This inadequate wetting leads to formation of voids that appear as pores at the braze/substrate interface, as the molten filler metal fails to flow and integrate smoothly across the joint interface. These small

voids/pores are formed due to the high viscosity of the molten filler material, which prevents it from spreading uniformly, a phenomenon exacerbated by the limited energy available for the fusion of filler wire. As the heat input increases, so does the energy transferred to the joint. Initially, the increased heat aids in reducing pore size by facilitating better wetting and flow of the molten metals leading to the defect-free condition (C_6). Further increases in the heat input, up to $\Delta HI_{Relative}$ = 4.36 J/mm (C_8), can prove counterproductive in the elimination of pores. Excessive energy input increases Zn vaporization, leading to the formation of large gas bubbles. The cooling rate at this level of heat input is high enough to prevent these bubbles from escaping the molten pool, resulting in pores with sizes exceeding the pore I.U.B. Interestingly, beyond a critical heat input threshold at $\Delta HI_{Relative}$ = 12.44 J/mm (C_9), there is a paradoxical reduction in pore size. The pores at this level remain below the pore I.U.B, similar to those formed at $\Delta HI_{Relative}$ = −3.42 J/mm (C_4), but they form through a different mechanism. At $\Delta HI_{Relative}$ = 12.44 J/mm (C_9), the excessive heat input melts not only the filler material, but also the base metal, altering the braze molten pool dynamics. While Zn vaporization and gas entrapment still occur, part of the energy is consumed by partial BMM formation. This leads to a balanced condition, where both the pores and BMM stay below the I.U.B. of both. Notably, partial base metal mixing introduces Fe-rich islands within the braze, which can enhance mechanical performance, as shown in a previous study [35].

Excessive heat input does not always result in progressive pore formation. At $\Delta HI_{Relative}$ = 22.54 J/mm (C_{11}), pore formation is suppressed due to several factors. The increased energy significantly reduces the viscosity of the molten filler, promoting complete substrate wetting. While Zn vaporizes progressively, the prolonged molten pool lifetime and reduced cooling rate provide gas bubbles with enough time to escape, minimizing gas entrapment. Additionally, dilution of the Zn coating reduces gas generation at the interface, further contributing to pore suppression. However, despite the elimination of pores, this high heat input causes excessive BMM, surpassing its I.U.B. and creating a defective condition.

3.3 Full-scale diagnosing of defect distribution within the braze seam using μCT

Among the various defect types, including LoA, pore, and BMM that formed in the brazing seam (as identified through MT and discussed above), the pore defect demonstrated a wide range of size variations under the different brazing conditions within the developed AI-friendly window.

LWB samples with pore defects are ideal candidates for μCT analysis due to their high frequency and the significant contrast between the pores (or voids) and the surrounding braze matrix in the μCT scans.

Four LWB conditions namely C_4, C_6, C_8, and C_9 with varying $\Delta HI_{Relative}$, that included a defect-free along with three pore conditions (both below and above the pore I.U.B. (0.2 mm diameter)), were selected for the pore analysis using the μCT results. Fig. 12a-d illustrates 2 cm sections of the μCT scanned results of actual braze seams generated under the different $\Delta HI_{Relative}$ conditions selected. To reveal the pore distribution along the corresponding braze seams, reduced opacity braze seams with pore distribution are depicted in Fig. 12e-h. Fig. 13 shows the corresponding distributions of the pore volume along the braze seam, measured from the top surface plane of the braze seam. The color coding in Fig. 12 and 13 represents the variations in the volume of pores. Pores of varying volumes and morphologies are distributed along the braze seam in all the selected samples. Notably, even the condition designated as defect-free (C_6) based on the MT results contains a variety of pores, although their size lay far below the pore I.U.B. (0.2 mm diameter), as shown in Fig. 13c. In LWB conditions with a pore size below the I.U.B. based on the MT results (e.g., C_4 and C_9), the μCT results shown in Fig. 13b reveal that the pores are more uniformly distributed compared to the condition with pores beyond the I.U.B. (C_8) (Fig. 13d). It should be noted that in C_8, μCT revealed two pores exceeding the pore I.U.B. per 2 cm length of the braze seam each 2 cm length of the braze seam. However, MT analysis could detect only one such pore across four cross-sections spaced 1 cm apart, meaning only one pore was identified over a 4 cm length. This comparison confirms that μCT captured approximately four times more critical pores than MT, highlighting the limitations of MT in detecting localized pore defects along the braze seam.

To statistically analyze the variations seen in the volumes of the pores formed along the braze seam of each condition, the whisker plot of individual pore volume across four selected conditions along 2 cm of the braze seam (Fig. 14a) and their corresponding distribution histograms were examined (Fig. 14b-e). The boxes in Fig. 14a show the range of pore volumes encompassing the 5^{th} to 95^{th} percentile pore volume. The whiskers in this plot indicates the 95% confidence interval (CI) for the mean pore volume for each selected $\Delta HI_{Relative}$ condition. Outliers are included in the quantification, as the AI-friendly specifications account for even a single defect exceeding the pore I.U.B. (0.2 mm diameter). From Fig. 14a, the $\Delta HI_{Relative}$=4.36

J/mm condition, which consisted of pores above the I.U.B. based on the MT results, showed the highest mean pore volume (1.57×10^{-3} mm^3) compared to other conditions. The mean pore volume in the other conditions (including the defect-free condition), ranged between 0.39-0.60 $\times10^{-3}$ mm^3. From the histogram of pore volumes in Fig. 14b-e, it can be deduced that pores below the I.U.B. (0.2 mm) are distributed evenly with a similar range of pore volumes. In contrast, pores exceeding the I.U.B. are few and not distributed uniformly through the seam.

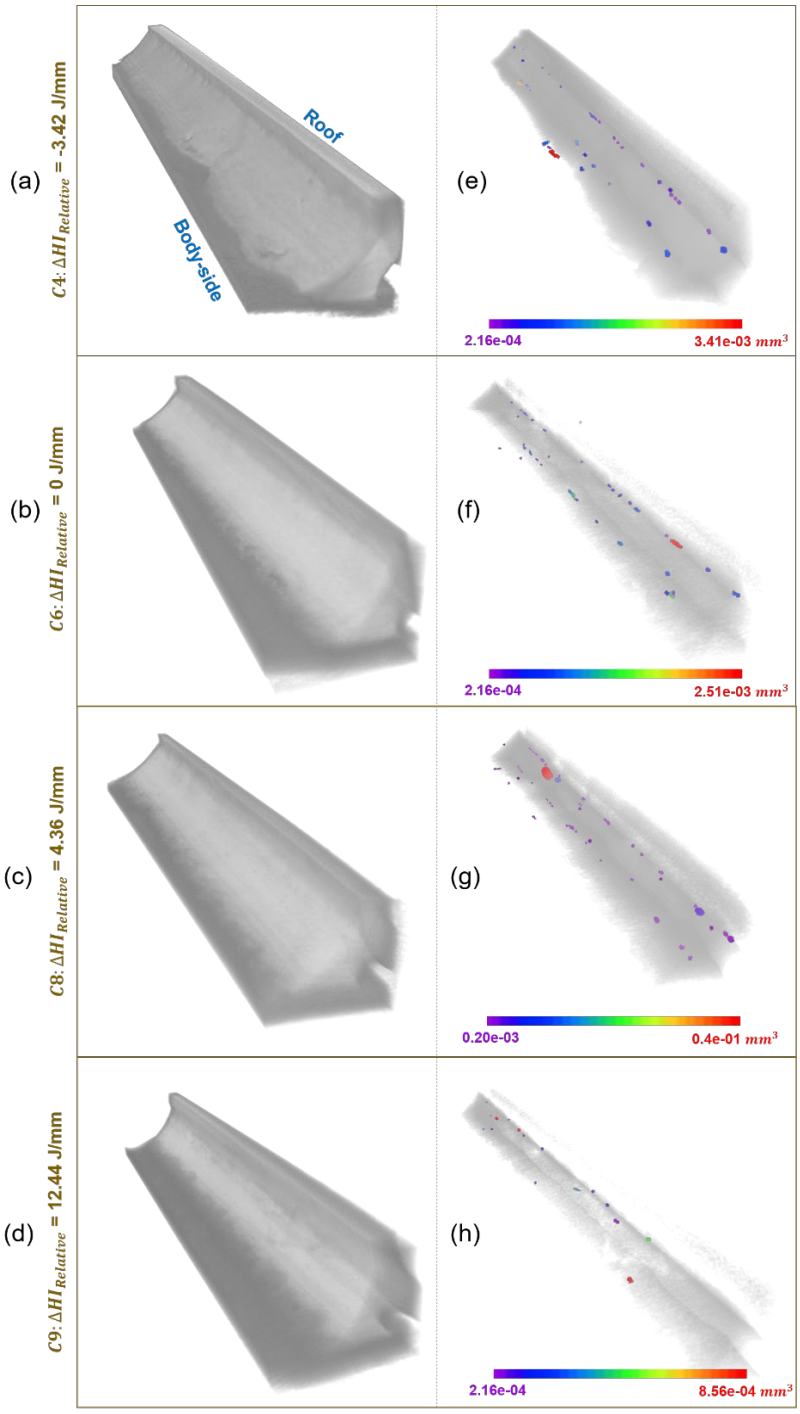


Fig. 12. (a-d) 3D visualization of representative 2 cm long braze seams of pore defect conditions with varying $\Delta HI_{Relative}$. The braze seam and substrates (roof and body-side parts) are distinguished by light grey and dark grey colors, respectively. (e-h) braze seams with reduced opacity, including pore distributions, in which the color-coding legend shows pore volume changes.

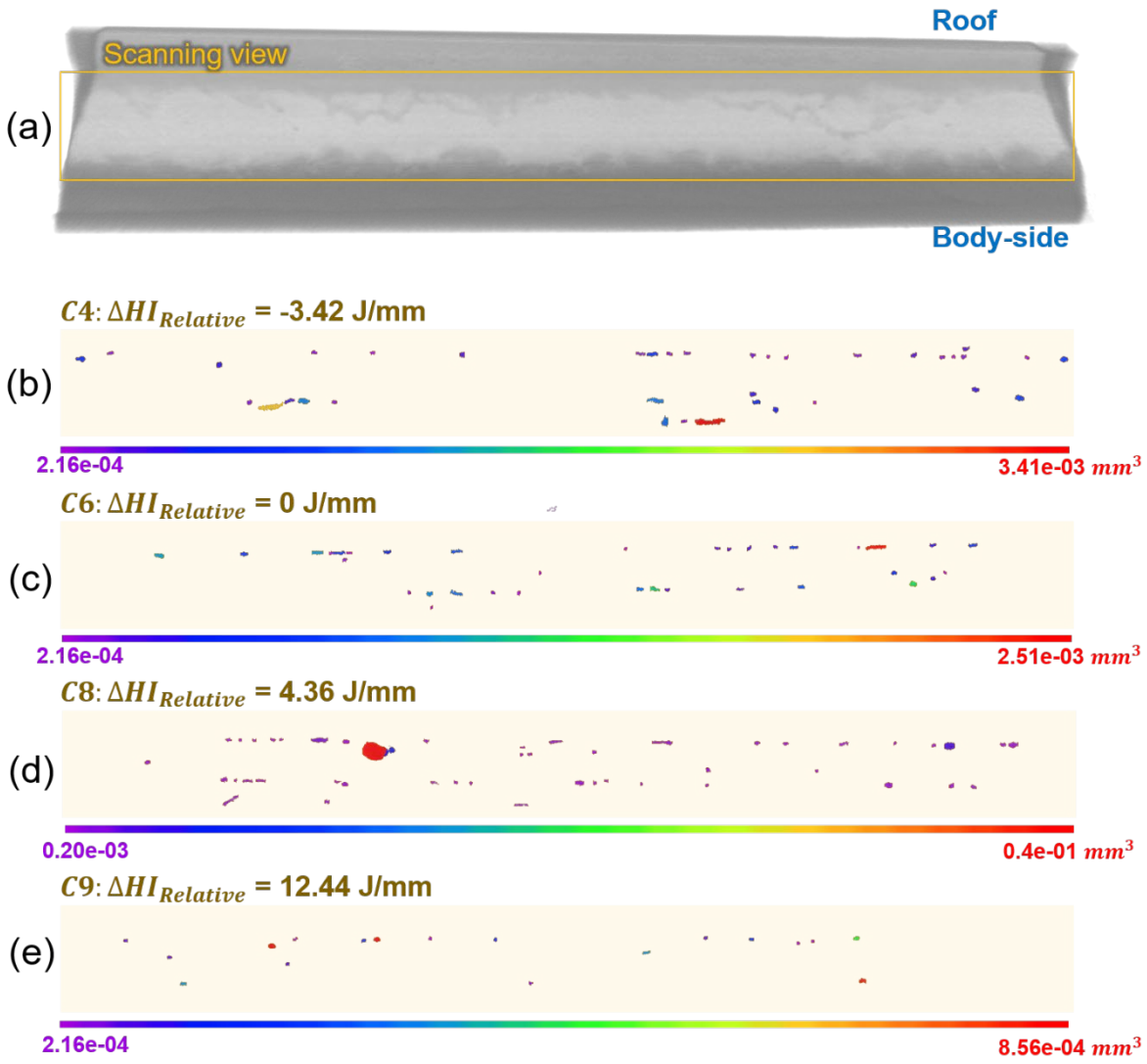


Fig. 13. (a) Top surface view of the µCT scanned braze seam. The yellow box shows the view plane for the pore volume distribution in 2D along the braze seams with varying $\Delta HI_{Relative}$ as given in (b-e).

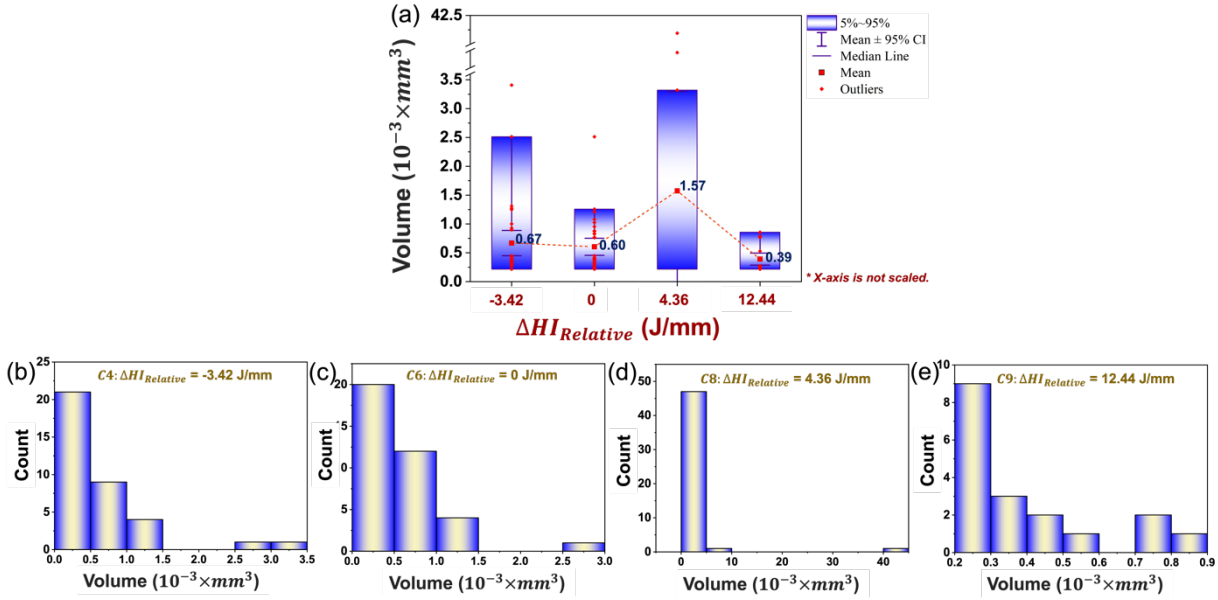


Fig. 14. (a) Whisker plot showing the quantification of the pore volume, and (b-e) their corresponding distribution histograms within the selected pore defect conditions with varying $\Delta HI_{Relative}$.

3.4 Generalization of optimization

To generalize the optimization based on pore analysis, it is essential to directly compare primary defect characterization results from MT with complementary defect analysis using µCT. Given that the pore diameter from the cross-sectional plane of the braze seams was included in the AI-friendly specifications, pore diameter measurements were also undertaken using µCT to ensure compatibility with the optimization criteria and comparability with the MT results. For this purpose, the Feret length, a parameter used in the post-processing module in the DragonFly software, was applied to measure the distance between any two points along the mesh boundary at an arbitrary angle of the occupied space by the targeted object—here, each pore—during the segmentation and analysis of the µCT data. For a single Feret, here pore, with irregular morphology, the lateral and longitudinal dimensions are defined as the minimum ($D_{min\ Feret}$) and maximum ($D_{max\ Feret}$) Feret diameters respectively. As the $D_{min\ Feret}/D_{max\ Feret}$ ratio approaches 1, the pore's morphology becomes more spherical; in this case, the pore diameter is equal to both the $D_{min.\ Feret}$ and $D_{max\ Feret}$. According to Fig. 13b-e, most pores with non-spherical morphology are elongated along the length of the braze seam, rather than in the lateral direction. Therefore, $D_{min\ Feret}$ is characterized as the pore diameter of interest in the AI-friendly specifications in the context of this study, determined from the cross-sectional plane of the braze seams, making it

comparable with the MT results. Fig. 15 illustrates the distribution of the pore diameter along the braze seam for each selected $\Delta HI_{Relative}$ condition, accompanied by the statistical analysis of the pore diameter presented in Fig. 16 (similar to the pore volume analysis in Fig. 13 and 14). From Fig. 16a, it is evident that pores in the condition with $\Delta HI_{Relative}$=4.36 J/mm have the highest mean diameter with 0.09 ± 0.05 mm compared to the other pore conditions. The mean pore diameter in the rest of the pore conditions, as well as the defect-free condition, are well below 0.08 ± 0.01 mm. The evolution of the pore diameter between the selected LWB conditions in Fig. 16a follows a similar trend to that of pore volume in Fig. 14a, in which the condition with $\Delta HI_{Relative}$=4.36 J/mm is considered as the condition with largest pores in terms of both the pore diameter and pore volume. It should be noted that the difference between the pore size, in the condition with $\Delta HI_{Relative}$=4.36 J/mm, is sharper in terms of the pore volume relative to the pore diameter. This is because the pore volume accounts for the pore size in all directions, while the pore diameter only compares its cross-sectional size. The MT results showed that the largest pore diameter detected within the selected conditions was 0.256 mm, while μCT revealed the presence of larger pores with a maximum diameter of 0.38 mm. Moreover, the pore diameter distribution for conditions with a $\Delta HI_{Relative}$ of –3.42 J/mm (Fig. 16; braze seam with pores below the I.U.B. detected in MT) and 0 J/mm (Fig. 16c; defect-free condition from MT) indicate that the pore diameters range from 0.06 mm to 0.12 mm and with approximately symmetrical bell-shaped distributions, suggesting that they are closer to a normal distribution within the presented 2 cm scans. In contrast, the other two conditions, $\Delta HI_{Relative}$ of 4.36 J/mm and 12.44 J/mm (Fig. 16d and e), show skewed distributions, indicating an uneven spread of pore sizes, which suggests localized variations in the pore formation rather than a normal distribution. These results, thus, recommend adding prudence to the optimization of any defect-free condition, such as C_6 with $\Delta HI_{Relative}$=0 J/mm, to account for the possibility of pores forming below the I.U.B.

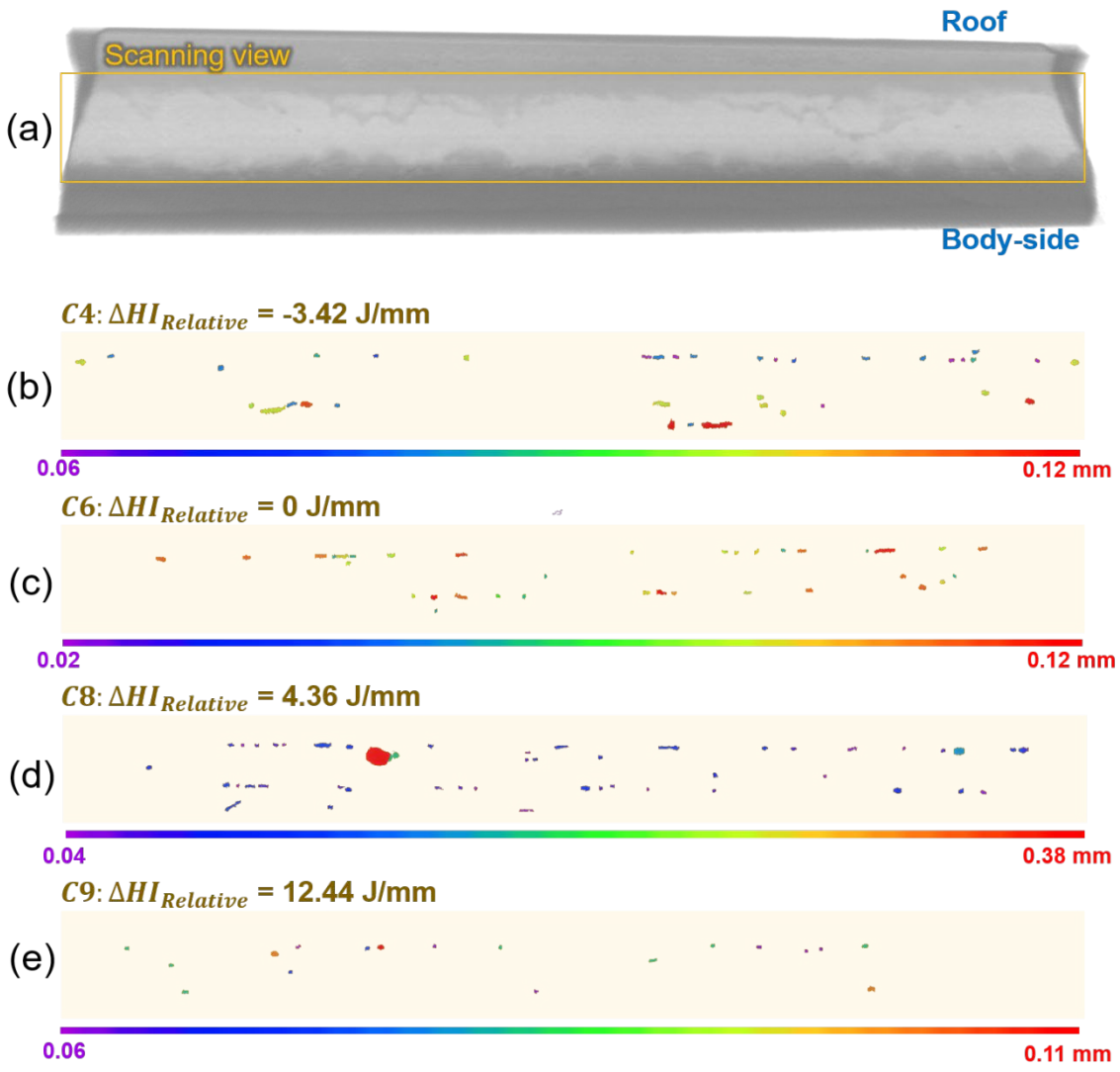


Fig. 15. (a) Top surface view of the μCT scanned braze seam shows the reference plane for 2D pore visualization. (b-e) pore diameter distribution along the braze seam of the pore defect conditions with varying $\Delta HI_{Relative}$.

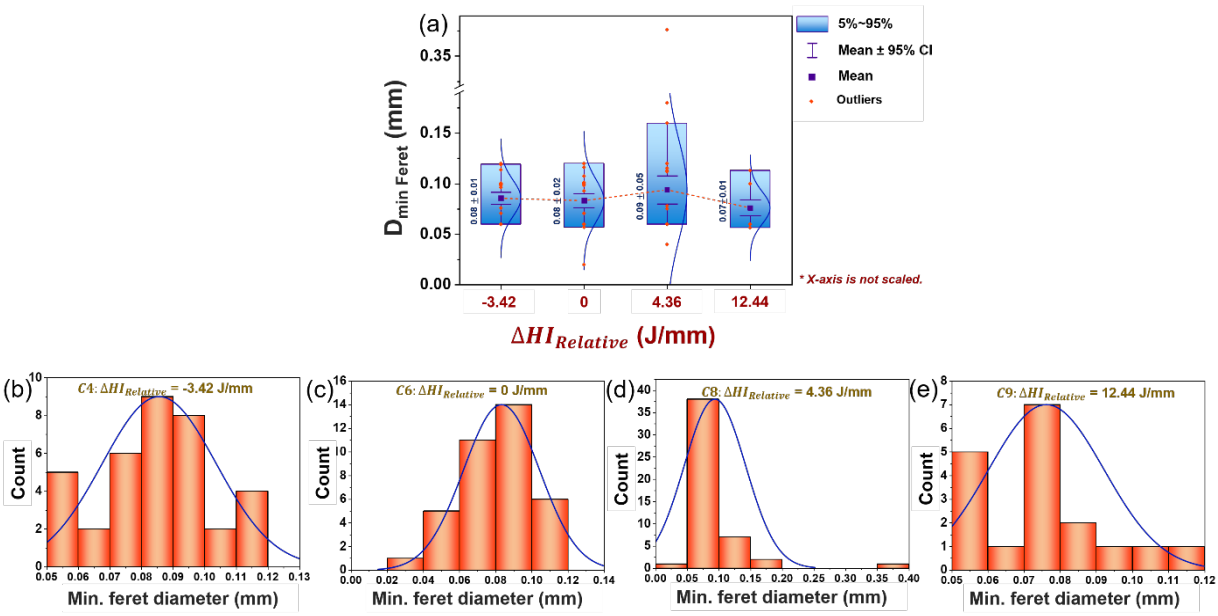


Fig. 16. (a) Whisker plot showing the quantification of the pore diameter ($D_{min\ Feret}$), and (b-e) their corresponding distribution histograms within the selected pore defect conditions with varying $\Delta HI_{Relative}$.

The µCT characterization confirmed that the primary defect analysis undertaken using MT remains valid for LWB optimization; however, the extent of its deviation from the exact full-scale analysis by µCT needs to be evaluated. For this purpose, a graph showing the correlation between the pore diameter and $\Delta HI_{Relative}$ values of the four selected conditions (pore and defect-free), for both the MT and µCT results, is depicted in Fig. 17. The metallography results are gathered as maximum (max), mean, and minimum (min) discrete linear curves of four points. The µCT results are shown by a purple polygonal domain that is defined based on considering the pore diameters within the lower 5% and upper 95% boundaries. Comparing the maximum pore diameter in the MT results and the upper 95% of pore diameters in the µCT, there is a deviation of approximately +0.12 mm in the MT results for both the defect-free braze joints and those with pores exceeding the I.U.B. conditions, respectively with $\Delta HI_{Relative}$ of 0 and 4.36 J/mm. Despite this deviation, it did not influence the classification of the pores according to the defect specifications. However, even in the conditions labeled as defect-free, it is important to consider that pores below the I.U.B., with diameters ranging from 0.02 to 0.12 mm, may still exist. Minimal deviation between the MT and µCT results, which did not alter the $\Delta HI_{Relative}$ boundaries for defining the various pore defect braze conditions, ensures consistency in the

classification of other defect conditions, such as LoA and BMM, for which quantification was not feasible using μCT due to difficulties in distinguishing these defects from the braze seam and base material. The contrast between BMM, the braze material, and the base metal is insufficient. In the case of LoA, it often merges with the natural gap at the braze root, making it indistinguishable from non-defective regions in μCT data.

Comparatively μCT scanning has so far been implemented to detect sub-surface defects in joints produced by laser welding [44], resistance spot welding [45], and friction stir welding [46], [47], primarily for enhancing quality control applications; these weld samples consisted of a single material and featured symmetrical, rectangular joint geometries, allowing pore analysis to be performed using the existing segmentation modules during post-processing. However, due to the challenges in pore segmentation of braze samples with dissimilarities in the geometry and material of the braze region and substrates, a full-scale demonstration of pore formation evolution along the braze seam had previously been overlooked. For the first time, this study could demonstrate that achieving highly accurate pore detection for braze joints is feasible through the use of semi-automatic segmentation. While semi-automatic segmentation of μCT data to identify pores within the braze seam might be perceived as time-consuming, it is still more efficient compared to MT, given the significantly longer sample preparation time required for the latter. Also, with MT, approximately 80% of the braze seam remains uncharacterized due to the bulk of the sample required for cutting and mounting.

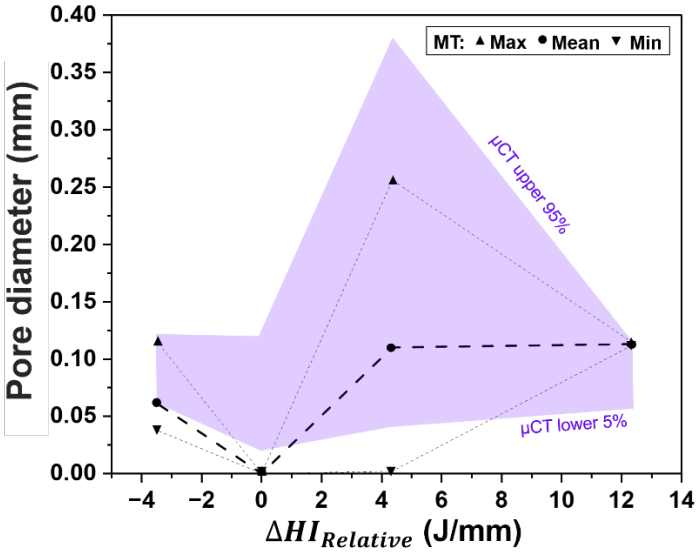


Fig. 17. Comparison of pore detection results characterized using MT and μCT methods.

This study is also the first to present the correlation between LWB process parameters, embedded in the $\Delta HI_{Relative}$ term, and pore evolution within the braze seam, validating process stability. The optimization strategy introduced—wire-adjusted heat input—demonstrates a scalable framework for other LWB applications involving similar substrates. The comprehensive μCT analysis conducted enabled 3D visualization and quantification of the pore evolution within the braze seam, providing valuable insights into the braze conditions and ensuring a thorough understanding of the process window's accuracy and reliability, which robustly validated the AI compatibility of braze joints produced using the proposed AI-friendly process window. The 2D slice outputs from the μCT scans of each braze seam were fed into the AI database required for real-time NDT training.

3.5 Performance of AI for joint geometry prediction from UT data

While MT provides physical verification, it is destructive and limited to a few planes, and μCT is time consuming and expensive to implement. For this purpose, AI-enhanced UT inspection, is needed to fully characterize the braze in a time-efficient and cost-effective manner, especially for industrial applications. To establish an automated sizing, alongside the detection of any indications of pores, LoA, BMM or other imperfections, a number of constraints need to be addressed. 1) Ultrasound imaging must be capable of seeing the defect; 2) The defect must be labeled in μCT data; 3) The UT and μCT data must be aligned properly. Among brazing defects,

pores present a technical challenge in the creation of such a training set as a result of their limited size, spherical shape, and the possibility of clustering. Ultrasonically, the size and shape of a pore limit the reflection amplitude such that mostly pores above the I.U.B. are expected to be visible. The smaller pore size requires a higher resolution of scanning along the direction of brazing to ensure detection. The evaluation of braze seams produced using the process window established in this work showed reliable signal feedback for defect detection and the geometry of the braze. Fig. 18 illustrates the µCT and UT images from the same location along the braze bead for a brazing condition containing pore defects within the process window, an example representing one of the most challenging cases for UT detection. The UT image shows an excellent visualization of the pores by the ultrasonic technique, and it perfectly matches with µCT data. It should be noted that the braze seams of all conditions, C_1 to C_{11}, have shown perfect fit for establishing AI-enhanced UT. Using rigid body image registration, these joints were then matched to within 0.1 mm of each other to allow for the creation of a baseline training set.

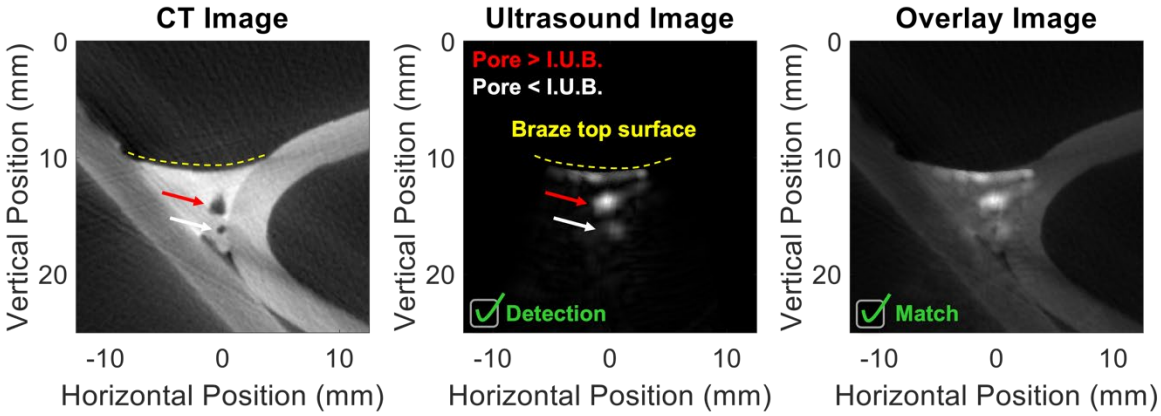


Fig. 18. Images of the same location along the braze bead of a sample produced at pore condition C_8, illustrating the match in pore locations and sizes, as seen in the enveloped UT and CT images. The visibility of the bottom surface is limited, as the pore obstructs the ultrasound path.

The semantic segmentation approach was conducted employing deep learning that was trained using the database derived from µCT scanning of the LWB joints with various defect conditions within the resulting window. Fig. 19 illustrates an example from condition C_8, showcasing the processing steps for both µCT-based ground truth extraction and UT-based evaluation using semantic segmentation AI. The µCT scans are processed to generate ground truth masks that delineate key features such as the joint, substrate, pores, and LoA. These masks provide detailed geometric data for the joint and substrate, which are aggregated and measured over a defined

window of μCT images. The UT data, including subsurface and surface scans, is then fed into a trained semantic segmentation model. This model predicts corresponding feature masks, and the resulting data is used to derive measurements for evaluation and comparison.

Given only the UT data, the semantic segmentation AI was able to identify joint geometry and substrate regions that strongly reflect those in the ground truth that was extracted from μCT. The semantic segmentation approach, employing deep learning, trained using the database derived from μCT scanning of the selected LWB joints, proved to be a reliable solution to extract actionable information about the joint geometry from the UT data. The semantic segmentation approach was used for this study over other possible options because it had the potential to produce high-resolution fine-grained mask outputs from which measurements could be straightforwardly derived. Conducting a more direct regression of the measurements given the UT data is possible, but the segmentation step provides an intermediate representation of the data that can be easily inspected by a human operator. This can be extremely beneficial, especially in cases where the extracted measurements exhibit variance along a joint or are outside of expected ranges. Additionally, the intermediate mask output can enhance the trustworthiness of the AI-based predictions, which is especially important in the context of NDT applications, as mask visualization can easily reveal biases in predictions, clear mismatch between input UT data and output masks, as well as catastrophic failures (e.g., due to ultrasonic hardware or electronics failures, vastly out-of-domain inputs, etc.). Although the semantic segmentation approach was proven to reliably extract joint geometries, the identification of pore, LoA, and BMM defect indications is relegated to future work.

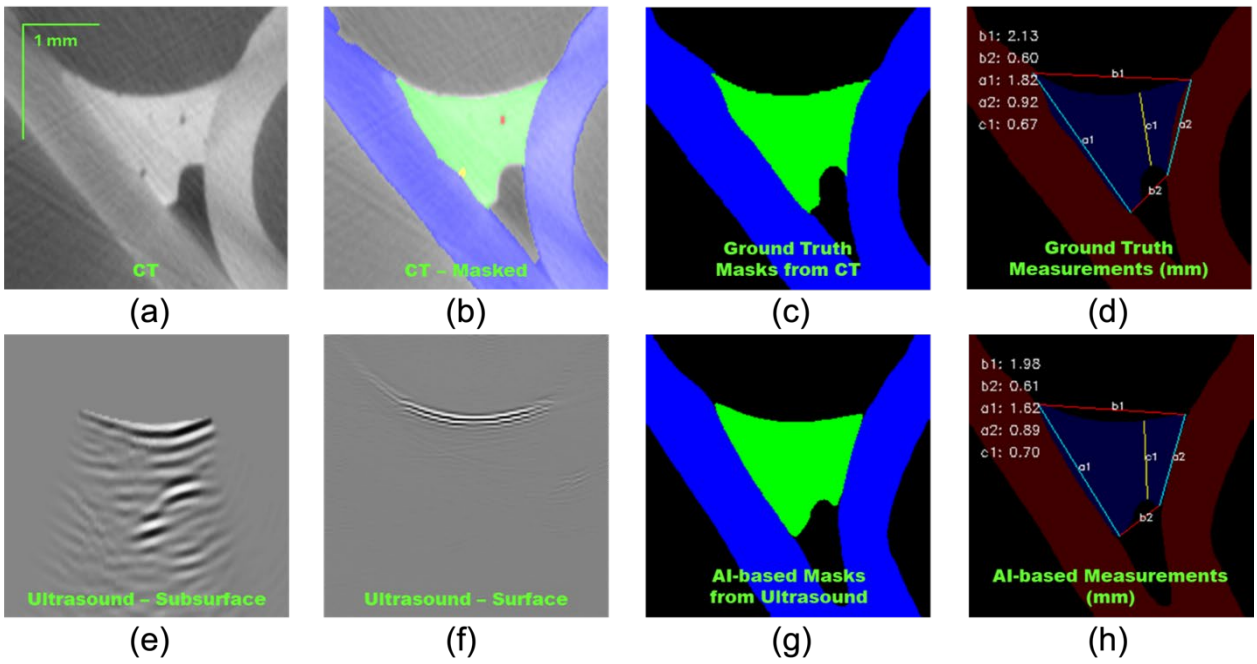


Fig. 19. (a-d) example from condition C_8 of processing of µCT for ground truth extraction, and (e-h) UT using semantic segmentation AI for joint evaluation. Original µCT scan (a) is processed (b) to extract ground truth masks for joint (green), substrate (blue), pores (red), and lack-of-adhesion (yellow). Joint (green) and substrate (blue) geometries from µCT are then aggregated from a window of µCTs (c) and measured (d). Ultrasonic subsurface (e) and surface (f) scans (only waveform images are shown here for brevity) are given to the trained segmentation model as inputs, and model outputs masks (g). Measurements are then derived from output mask data (h).

The AI mask outputs from UT data aligned strongly with µCT-based ground truth masks, which enabled reliable and straightforward measurement extraction from individual UT scans. Acquiring and subsequently processing the UT scans taken consecutively, either in real-time as they are acquired or offline, enables the automatic extraction of measurements at high sampling rates along LWB joints as shown for condition C_8 in Fig. 20. In this work, the UT sampling was conducted at 0.1 mm intervals along the joint, but in practice the movement of the UT probe can be modulated based on the needs of the user. Additionally, with this approach, extracted measurements can automatically be subjected to joint acceptance criteria downstream, defined by users according to their needs or standards. Integration of the ultrasonic probe and electronics, as well as AI-driving software and the necessary computing hardware, into a robotic inspection system enables a fully automated ultrasonic NDT solution for LWB joints. In condition *C8* (Fig. 20), there was a slight bias of the predictions for a1 (left leg in Fig. 19) and b1 (front face in Fig. 19) compared to ground truth, but this was not consistently observed in other samples. This is

possibly due to the relatively small number of the nominal samples (20 LWB joints, each containing 900 µCT–UT matched data points, resulting in ~18,000 data pairs in total), which may lead to misjudgement by the AI either on held-out samples during nested cross-validation or on regions of the joints demonstrating particular conditions, and may be rectified by scaling up the approach for data collection. Nonetheless, the extracted measurements provide a reliable judgement of joint geometry across the joint and demonstrate that it is possible to semi or fully automate a complete LWB joint analysis using ultrasound supported by AI. To further validate the approach, probability-of-detection and probability-of-false alarm analyses based on extracted measurements and joint acceptance criteria should be conducted in future work.

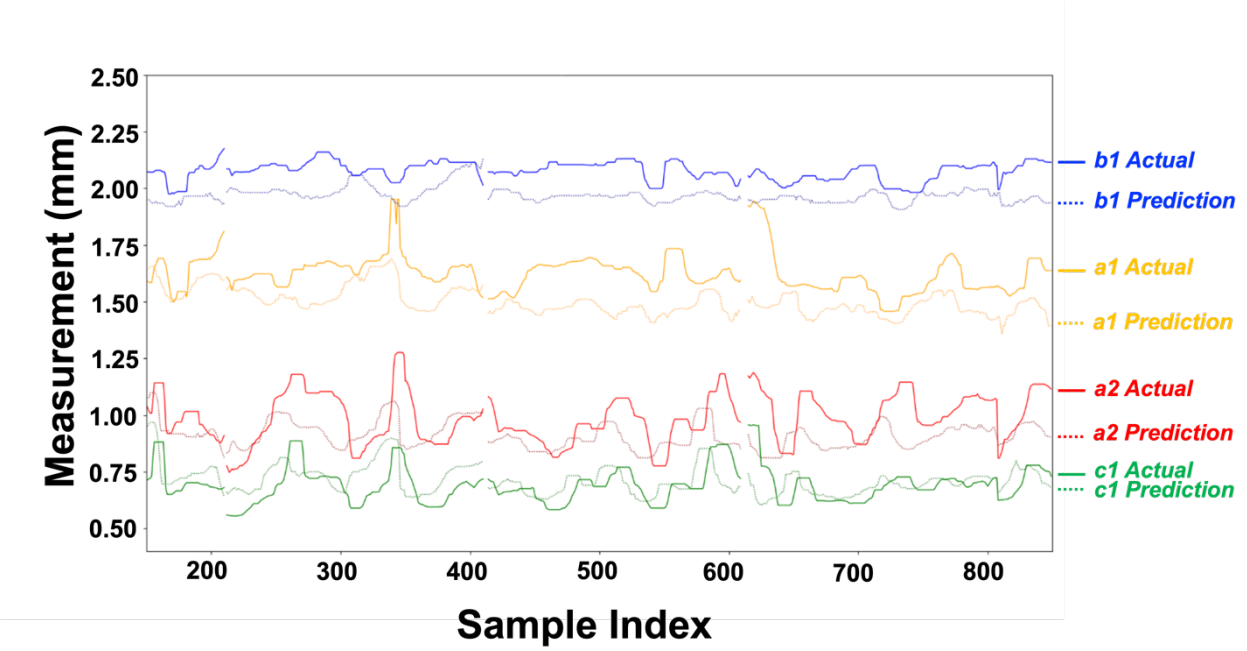


Fig. 20. Joint geometry measurements extracted from µCT data ("Actual"), as well as UT data using segmentation AI ("Prediction"), along the length of sample C8. All joints yielded 1000 UT samples, but first and last 150 measurements were excluded, and gaps in data existed at sample indices 200, 400, 600, and 800, due to edge effects in µCT scanning.

The process window developed in this work produced a set of samples with sufficient consistency within the joints and variance across the joints to support the development of AI for automated high-performance prediction of joint geometry from UT data. The MT measurements demonstrated greater variance as there was a relatively small sample size (n=4 per joint sample; Table 5). Across the four cross-sections from each joint sample, c1 (bridge height) and a2 (right leg) measurements were most consistent between the MT and µCT, while a1 (left leg) and b1

(front face) measurements showed greater variance in MT and greater discrepancy between MT and μCT (Fig. 21a). The greater discrepancy between MT and μCT for a1 and b1 indicates that braze seam formation along these dimensions experienced the highest instability, driven by altered wetting of the molten braze on the sloped body-side substrate during seam formation. There was very little discrepancy between the measurements derived from μCT and UT using the AI approach (Fig. 21b), which was expected as the AI was trained to model a function from UT data inputs to mask outputs that were derived from μCT scans. This demonstrates that the performance of the semantic segmentation AI, using a supervised deep learning approach, highly depends on the quality of its ground truth data (in this case, masks derived from μCT). The developed process window produced samples with MT a1 (left leg) measurements ranging from 1.330 mm to 2.270 mm, a2 (right leg) measurements ranging from 0.770 mm to 1.170 mm, b1 (front face) measurements ranging from 2.090 mm to 2.650 mm, and c1 (bridge height) measurements ranging from 0.590 mm to 0.830 mm, while standard error of the MT measurements ranged from 6.02% to 34.70% overall. The low variance within a LWB joint demonstrated the stability of the identified process parameters, and this contributed to the amenability of the joint to be inspected, including ultrasonically. Additionally, subtle variance along the joint, including minor changes in joint geometry as well as localized presence of pores and other purposely-induced defects, contributed to the robustness and coverage of the resultant ultrasonic dataset, and this helped to reduce epistemic uncertainty in the AI development process. The broad range of measurements and geometric variations across the manufactured joints established control over the process, which was afforded by the developed process window. This was crucial for maximizing ultrasonic dataset coverage that further reduced epistemic uncertainty in the AI development process. Ultimately, this work demonstrates a process window which is ideal for creating a dataset, which can be used for the development of an end-to-end AI system to automate the ultrasonic inspection and evaluation of LWB joints.

Table 5. Extracted measurements from the MT, CT, and AI on the UT data, averaged for 2 cm length of the braze seam, with standard error (SE) calculated using 95% confidence interval (CI).

Measurement	Condition Name	MT (mm)	MT SE (mm)	CT (mm)	CT SE (mm)	AI (mm)	AI SE (mm)
a1	C4	1.33	0.28	1.167	0.007	1.176	0.005
	C6	1.83	0.23	1.800	0.008	1.673	0.007
	C8	2.11	0.17	1.617	0.008	1.507	0.007
	C9	2.27	0.43	1.353	0.007	1.382	0.008
a2	C4	0.77	0.10	0.657	0.004	0.690	0.004
	C6	1.11	0.16	1.248	0.005	1.176	0.005
	C8	1.16	0.20	0.985	0.009	0.915	0.006
	C9	1.17	0.37	0.866	0.005	0.771	0.006
b1	C4	2.09	0.25	1.696	0.006	1.640	0.004
	C6	2.41	0.22	2.297	0.006	2.179	0.005
	C8	2.50	0.34	2.062	0.005	1.968	0.003
	C9	2.65	0.51	1.607	0.006	1.663	0.004
c1	C4	0.59	0.09	0.487	0.002	0.553	0.002
	C6	0.72	0.25	0.962	0.005	0.966	0.005
	C8	0.83	0.05	0.692	0.007	0.717	0.006
	C9	0.78	0.26	0.587	0.004	0.593	0.005

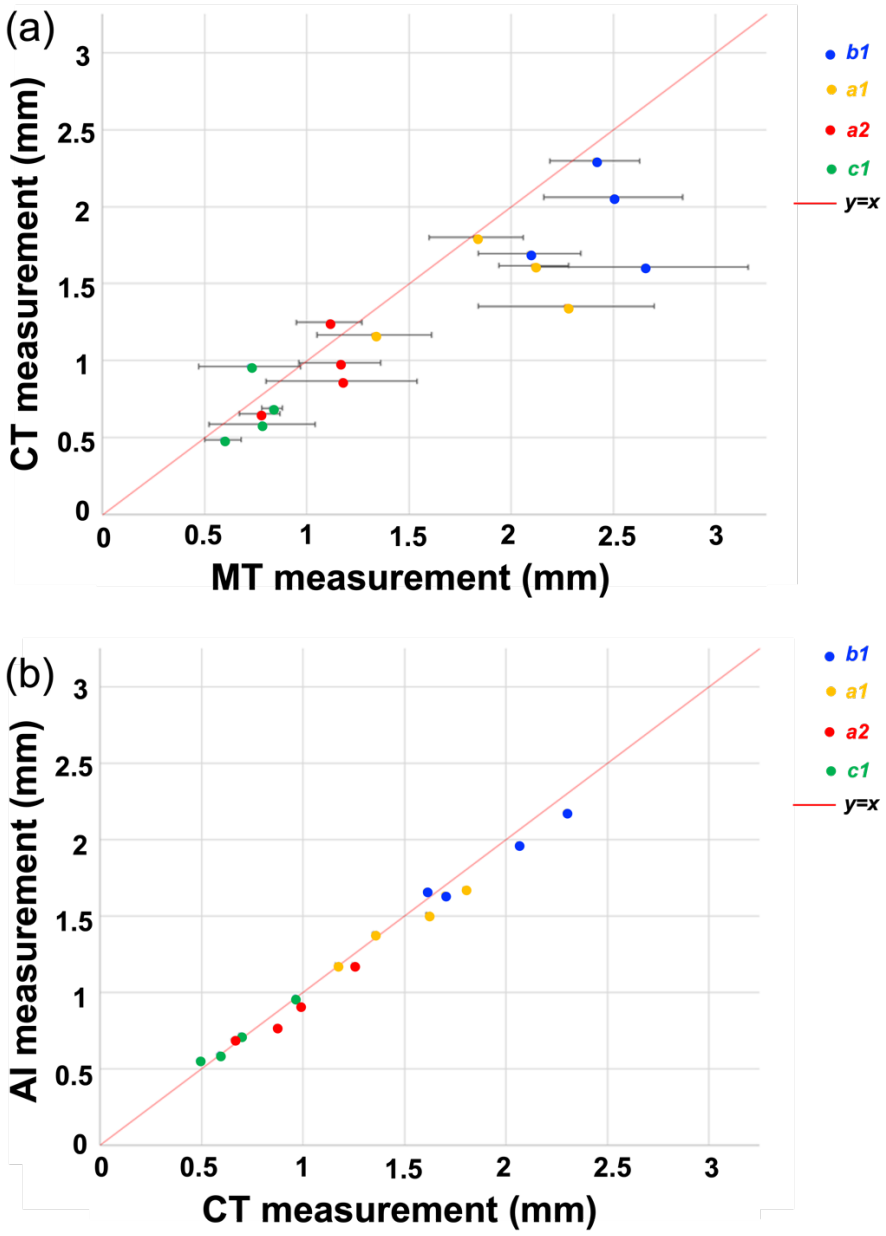


Fig. 21. Comparison of MT and μCT measurements (a), as well as μCT and AI-based measurements from UT (b) for brazing conditions C_4, C_6, C_8, and C_9. Both vertical and horizontal error bars are shown on both graphs, but errors are too small to visualize for μCT and AI outputs due to both high sample size and measurements consistency.

Conclusions

This study highlighted advancements in laser-based manufacturing, focusing on process optimization and defect control in robotic laser weld brazing (LWB). The integration of artificial intelligence (AI) played a key role in automating defect detection and joint geometry prediction

from ultrasonic testing (UT) data. Advanced characterization with micro-computed tomography (μCT) scanning provided essential ground truth for training AI models and understanding defect evolution. These elements were integrated into an AI-driven quality assurance framework, significantly improving the reliability and automation of feasible in-plant non-destructive testing (NDT) of laser processing in industrial applications. The main conclusions can be listed as follows:

1- A custom-designed process window was established which is capable of producing braze seams with the various defect classes required for AI training of an industrial-level real-time ultrasonic technique for defect detection.

2- The conventional heat input parameter, $HI_{Nominal}$, correlated with brazing defects only at a constant wire feed speed (WFS). As this relationship did not hold when WFS was varied, a novel wire-adjusted heat input approach was proposed to find a direct correlation between HI and defect formation.

3- The HI-related boundaries determined from the novel wire-adjusted heat input approach facilitated LWB optimization by distinguishing the required HI for producing a defect-free braze seam, as well as braze seams with defects such as: lack of adhesion, pores and base metal melting below and above the specified imperfection upper bound for each defect type.

4- A full-scale defect analysis via μCT scanning along the length of braze seams with and without various defects was conducted as a complementary defect characterization technique to the preliminary metallography technique (MT). It was confirmed that the presence of pores with the required diameter was highly repeatable along the braze seams; this proved the robustness of the boundaries identified by the wire-adjusted heat input approach for each defect condition.

5- Comparing maximum pore diameter in MT and upper 95% of pore diameters in μCT showed a small deviation of about +0.12 mm for the defect-free braze and braze conditions containing pores above the pore I.U.B. (0.2 mm diameter). This deviation did not affect labeling the pore conditions according to the defect classes. However, even in a defect-free labeled condition, pores below the I.U.B. may still be present.

6- The process window effectively ensured stable and controlled LWB joint production of the varied joint qualities needed for AI training, enabling reliable UT detection of the seam geometry and defect conditions.

7- The deep learning-based semantic segmentation model developed in this study demonstrated strong performance in identifying key joint features, such as seam geometry and substrate boundaries from UT data. The model output provided accurate and consistent measurement extraction, supporting reliable geometric evaluation of LWB joints across varied brazing conditions.

8- By leveraging high-resolution ground truth from μCT and aligning it with UT data using rigid registration, this study enabled the development of a supervised deep learning framework capable of automated joint geometry extraction with high fidelity. The intermediate mask output provided explainability and operator validation, demonstrating how AI tools can be integrated into fully automated, real-time ultrasonic NDT systems for brazed joints. Future extensions may enable full defect classification and support probability-based quality assessment.

Funding

This research was funded by the National Research Council Canada as part of the Canada – Germany 3+2 Research Collaboration on Smart Solution for Quality Control of Vehicle Assembly using an Ultrasonic Imaging Sensor with Embedded Artificial Intelligence under Grant# NRC INT-018-1.

Acknowledgments

The authors would like to acknowledge the financial support from the National Research Council (NRC) of Canada. The X-ray micro-computed tomography (μCT) scanning was performed at the Multi-Scale Additive Manufacturing Lab (MSAM) at the University of Waterloo.

Appendix A. List of Abbreviations

Abbreviation	Definition
BMM	Base Metal Melting
CI	Confidence Interval
DL	Deep Learning
HI	Heat Input
$HI_{Nominal}$	Nominal Heat Input
$HI_{Relative}$	Relative Heat Input
HI_{Wire}	Wire Heat Input
I.U.B	Imperfection Upper Bound
LoA	Lack of Adhesion
LWB	Laser Weld Brazing
ML	Machine Learning
MT	Metallography Technique
OM	Optical Microscope
P	Power
ROI	Region Of Interest
Thr.	Threshold
TS	Travel Speed
UT	Ultrasonic Testing
WFS	Wire Feeding Speed
μCT	Micro-Computed Tomography

References

[1] D. Krishnaja, M. Cheepu, D. Venkateswarlu, A review of research progress on dissimilar laser weld-brazing of automotive applications, IOP Conf Ser Mater Sci Eng 330 (2018) 0–16. https://doi.org/10.1088/1757-899X/330/1/012073.

[2] A. Koltsov, L. Cretteur, Wetting and interfacial reactivity of Zn-Coated steel products with Cu-Si, Cu-Sn and Al-Si Filler metals for laser brazing application, J Mater Eng Perform 27 (2018) 5002–5010. https://doi.org/10.1007/s11665-018-3304-z.

[3] Y. Li, C. Chen, R. Yi, Y. Ouyang, Review: Special brazing and soldering, J Manuf Process 60 (2020) 608–635. https://doi.org/10.1016/j.jmapro.2020.10.049.

[4] R.W. Messler, Trends in key joining technologies for the twenty-first century, Assembly Automation 20 (2000) 118–128. https://doi.org/10.1108/01445150010321733.

[5] S. Akbarian, M.S. Khan, O. Sherepenko, M. Lee, P. Wanjara, E. Biro, Effect of heat source and Zn-coating type on the geometry and morphology of laser-brazed thin-gauge steels, J Manuf Process 107 (2023) 356–367. https://doi.org/10.1016/j.jmapro.2023.10.049.

[6] Y.H. Cho, M. Shehryar Khan, F.E. Goodwin, Y.N. Zhou, Effect of torch angle and position on bead geometry and joint strength during arc brazing of thin gauge dual-phase steel, International Journal of Advanced Manufacturing Technology 121 (2022) 543–557. https://doi.org/10.1007/s00170-022-09309-7.

[7] M. Shehryar Khan, Y. Norman Zhou, Weld-brazing or welding-brazing: Addressing the inconsistency in the naming convention used for this transformative non-fusion joining technique, Manuf Lett 36 (2023) 44–45. https://doi.org/10.1016/j.mfglet.2023.02.002.

[8] K.M. Hong, Y.C. Shin, Prospects of laser welding technology in the automotive industry: A review, J Mater Process Technol 245 (2017) 46–69. https://doi.org/10.1016/j.jmatprotec.2017.02.008.

[9] F. Klocke, S. Frank, Surface deposits in laser brazing, Science and Technology of Welding and Joining 18 (2012) 62–69. https://doi.org/10.1179/1362171812Y.0000000075.

[10] H. Traxler, W. Arnold, W. Knabl, P. Rödhammer, Non-destructive evaluation of brazed joints by means of acoustic emission, J. Acoustic Emission 20 (2002) 257.

[11] A. Ouellette, Adaptive, High-Resolution Ultrasound Phased Array Imaging for use in the Inspection of Laser Brazed Joints in the Automotive Sector, Degree of Doctor of Philosophy at, University of Windsor, 2020. https://scholar.uwindsor.ca/etd/8325.

[12] M.A. Machado, L.F.S.G. Rosado, N.A.M. Mendes, R.M.M. Miranda, T.J.G. dos Santos, New directions for inline inspection of automobile laser welds using non-destructive testing, International Journal of Advanced Manufacturing Technology 118 (2022) 1183–1195. https://doi.org/10.1007/s00170-021-08007-0.

[13] S. Sattarpanah Karganroudi, A. Aminzadeh, V.B.F. Kemda, N. Barka, 3D hardness profile mapping and geometrical defect prediction of laser-welded galvanized steel blanks using wobbling technology: an experimental investigation, International Journal of Advanced Manufacturing Technology 120 (2022) 2229–2246. https://doi.org/10.1007/s00170-022-08930-w.

[14] M. Ungers, D. Fecker, S. Frank, D. Donst, V. Märgner, P. Abels, S. Kaierle, In-situ quality monitoring during laser brazing, Phys Procedia 5 (2010) 493–503. https://doi.org/10.1016/j.phpro.2010.08.077.

[15] Y. Rong, G. Zhang, Y. Chang, Y. Huang, Integrated optimization model of laser brazing by extreme learning machine and genetic algorithm, International Journal of Advanced Manufacturing Technology 87 (2016) 2943–2950. https://doi.org/10.1007/s00170-016-8649-6.

[16] M.A. Machado, L.S. Rosado, N.M. Mendes, R.M. Miranda, T.G. Santos, Multisensor inspection of laser-brazed joints in the automotive industry, Sensors 21 (2021) 7335. https://doi.org/10.3390/s21217335.

[17] S. Hua, B. Li, L. Shu, P. Jiang, S. Cheng, Defect detection method using laser vision with model-based segmentation for laser brazing welds on car body surface, Measurement (Lond) 178 (2021) 109370. https://doi.org/10.1016/j.measurement.2021.109370.

[18] M.R.Gr. Scott R., Stocco D., Chertov A., Real-time AI-driven interpretation of ultrasonic data from resistance spot weld process monitoring for adaptive welding, Artificial Intelligence and Machine Learning in NDT, Mater Eval 81 (2023) 61–70. https://doi.org/https://doi.org/10.32548/2023.me-04344.

[19] M. Rudolph, B. Wandt, B. Rosenhahn, Same but DifferNet: Semi-supervised defect detection with normalizing flows, Proceedings - 2021 IEEE Winter Conference on

Applications of Computer Vision, WACV 2021 (2021) 1906–1915. https://doi.org/10.1109/WACV48630.2021.00195.

[20] M. David Jedrusiak, F. Weichert, A Deep Learning Approach for Denoising Air-Coupled Ultrasonic Responds Data, International Journal of Artificial Intelligence & Applications 11 (2020) 15–28. https://doi.org/10.5121/ijaia.2020.11402.

[21] D. Medak, L. Posilović, M. Subašić, M. Budimir, S. Loncaric, DefectDet: A deep learning architecture for detection of defects with extreme aspect ratios in ultrasonic images., Neurocomput 473 (2022) 107–115. https://doi.org/https://doi.org/10.1016/j.neucom.2021.12.008.

[22] M.R.Gr. Scott R., Stocco D., Chertov A., Using deep learning to characterize ultrasonic B-scans., in: ASNT Research Symposium 2022 Proceedings, 2022.

[23] J. Nowroth, C.; Gu, T.; Grajczak, J.; Nothdurft, S.; Twiefel, J.; Hermsdorf, J.; Kaierle, S.; Wallaschek, Deep Learning-Based Weld Contour and Defect Detection from Micrographs of Laser Beam Welded Semi-Finished Products, Appl. Sci. 12 (2022) 4645. https://doi.org/https://doi.org/10.3390/app12094645.

[24] A. Tyystjärvi, T., Fridolf, P., Rosell, Deploying Machine Learning for Radiography of Aerospace Welds, J Nondestruct Eval 43 (2024). https://doi.org/https://doi.org/10.1007/s10921-023-01041-w.

[25] S. Cantero-Chinchilla, P.D. Wilcox, A.J. Croxford, Deep learning in automated ultrasonic NDE – Developments, axioms and opportunities, NDT and E International 131 (2022) 102703. https://doi.org/10.1016/j.ndteint.2022.102703.

[26] I. Virkkunen, T. Koskinen, O. Jessen-Juhler, J. Rinta-aho, Augmented Ultrasonic Data for Machine Learning, J Nondestr Eval 40 (2021) 1–11. https://doi.org/10.1007/s10921-020-00739-5.

[27] M. Gatzen, T. Radel, C. Thomy, F. Vollertsen, Wetting and solidification characteristics of aluminium on zinc coated steel in laser welding and brazing, J Mater Process Technol 238 (2016) 352–360. https://doi.org/10.1016/j.jmatprotec.2016.07.026.

[28] M. Lou, W. Cai, J. Huang, H.P. Wang, Y. Li, B.E. Carlson, M.G. Poss, Simulation of laser brazing of sheet panels and parametric studies of thermally-induced distortion reduction, J Manuf Process 60 (2020) 1–10. https://doi.org/10.1016/j.jmapro.2020.10.030.

[29] M.K. Jeon, W.B. Kim, G.C. Han, S.J. Na, A study on heat flow and temperature monitoring in the laser brazing of a pin-to-plate joint, J Mater Process Technol 82 (1998) 53–60. https://doi.org/10.1016/S0924-0136(98)00020-X.

[30] H. Xia, W. Tao, L. Li, C. Tan, K. Zhang, N. Ma, Effect of laser beam models on laser welding–brazing Al to steel, Opt Laser Technol 122 (2020) 105845. https://doi.org/10.1016/j.optlastec.2019.105845.

[31] Y. Jin, S. Jiahao, G. Chenkai, Z. Yixuan, L. Hongbing, J.P. Ovliera, T. Caiwang, Y. Zhishui, Effect of heat input on interfacial microstructure, tensile and bending properties of dissimilar Al/steel lap joints by laser Welding-brazing, Opt Laser Technol 142 (2021) 107218. https://doi.org/10.1016/j.optlastec.2021.107218.

[32] X. Zhao, H. Yang, A. Gerlich, Y.N. Zhou, High-deposition laser brazing with enhanced surface quality, bridge performance and mechanical properties, J Manuf Process 124 (2024) 38–51. https://doi.org/10.1016/j.jmapro.2024.05.078.

[33] X. Zhao, H. Yang, A. Gerlich, Y.N. Zhou, The influence of joint geometry on the interfacial bonding in laser-brazed flare joints of automotive steels, Manuf Lett 41 (2024) 33–37. https://doi.org/10.1016/j.mfglet.2024.07.002.

[34] J. Yang, J.P. Oliveira, Y. Li, C. Tan, C. Gao, Y. Zhao, Z. Yu, Laser techniques for dissimilar joining of aluminum alloys to steels: A critical review, J Mater Process Technol 301 (2022). https://doi.org/10.1016/j.jmatprotec.2021.117443.

[35] S. Akbarian, A. Salandari-rabori, S. Sarafan, P. Wanjara, J. Gholipour, A.R.H. Midawi, E. Biro, Tailoring intermetallic compound formation within laser weld brazed joints using a novel heat input approach, Journal of Materials Processing Tech. 334 (2024) 118622. https://doi.org/10.1016/j.jmatprotec.2024.118622.

[36] G. Wang, J. Shen, S. Liu, C. Jiang, X. Qin, Three-dimensional modeling and analysis of macro-pore structure of coal using combined X-ray CT imaging and fractal theory, International Journal of Rock Mechanics and Mining Sciences 123 (2019) 104082. https://doi.org/10.1016/j.ijrmms.2019.104082.

[37] P.J. Withers, C. Bouman, S. Carmignato, V. Cnudde, D. Grimaldi, C.K. Hagen, E. Maire, M. Manley, A. Du Plessis, S.R. Stock, X-ray computed tomography, Nature Reviews Methods Primers 1 (2021). https://doi.org/10.1038/s43586-021-00015-4.

[38] C.T.C. Inc., Dragonfly, (n.d.). https://www.theobjects.com/dragonfly.

[39] R.M. A. Ouellette, S Titov, B. Ghaffari, E. Hetrick, Full Matrix Capture for Ultrasonic Imaging through Brazed Surfaces, in: 26th ASNT Research Symposium, 2017.

[40] G. Dao, R. Ginzel, New customizable phased array UT instrument opens door for furthering research and better industrial implementation, AIP Conf Proc 1581 33 (2014) 164–170. https://doi.org/10.1063/1.4864816.

[41] T. Ronneberger, O., Fischer, P., & Brox, U-Net: Convolutional Networks for Biomedical Image Segmentation, in: Medical Image Computing and Computer-Assisted Intervention, 2015.

[42] S. Akbarian, A. Salandari-rabori, D.C. Ramachandran, S. Sarafan, P. Wanjara, J. Gholipour, A.R.H. Midawi, E. Biro, Disentangling the Failure Response of Various Intermetallic Compounds with Surrounded Interface Formed During Laser-Weld-Brazing Process, Metall Mater Trans A 56 (2025) 5152–5176. https://doi.org/10.1007/s11661-025-07951-w.

[43] M. Mazar Atabaki, J. Ma, W. Liu, R. Kovacevic, Pore formation and its mitigation during hybrid laser/arc welding of advanced high strength steel, Mater Des 67 (2015) 509–521. https://doi.org/10.1016/j.matdes.2014.10.072.

[44] M. Schmoeller, C. Stadter, M.K. Kick, C. Geiger, M.F. Zaeh, A novel approach to the holistic 3d characterization of weld seams—paving the way for deep learning-based process monitoring, Materials 14 (2021) 6928. https://doi.org/10.3390/ma14226928.

[45] S.C. Han, H.M. Park, S.H. Uhm, D.Y. Choi, H.C. Jeong, Y.J. Kim, T.S. Jun, Evaluation of liquid metal embrittlement crack in resistance spot welds under intensive welding condition using industrial X-ray computed tomography and machine learning, Welding in the World 65 (2021) 1887–1897. https://doi.org/10.1007/s40194-021-01109-z.

[46] R.B. Roy, A. Ghosh, S. Bhattacharyya, R.P. Mahto, K. Kumari, S.K. Pal, S. Pal, Weld defect identification in friction stir welding through optimized wavelet transformation of signals and validation through X-ray micro-CT scan, International Journal of Advanced Manufacturing Technology 99 (2018) 623–633. https://doi.org/10.1007/s00170-018-2519-3.

[47] R.F. Hamade, A.M.R. Baydoun, Nondestructive detection of defects in friction stir welded lap joints using computed tomography, Mater Des 162 (2019) 10–23. https://doi.org/10.1016/j.matdes.2018.11.034.